X-ray transparent Microfluidics for Protein Crystallization and Biomineralization

A Dissertation

Presented to

The Faculty of the Graduate School of Arts and Sciences

Brandeis University

Physics Department

Seth Fraden, Advisor

In Partial Fulfillment

of the Requirements for the Degree

Doctor of Philosophy

by

Achini Opathalage

February, 2016

The signed version of this form is on file in the Graduate School of Arts and Sciences.

This dissertation, directed and approved by Achini Opathalage's committee, has been accepted and approved by the Graduate Faculty of Brandeis University in partial fulfillment of the requirements for the degree of:

DOCTOR OF PHILOSOPHY

Eric Chasalow, Dean
Graduate School of Arts and Sciences

Dissertation Committee:
Seth Fraden, Chair
Zvonimir Dogic, Physics Department
Dagmar Ringe, Biochemistry Department

To my parents.

Acknowledgments

Sincere gratitude to my Advisor

Many thanks to all whom I learned from and worked with

Heartiest appreciation of my family

Abstract

X-ray transparent Microfluidics for Protein Crystallization and Biomineralization

A dissertation presented to the Faculty of
the Graduate School of Arts and Sciences of
Brandeis University, Waltham, Massachusetts

by Achini Opathalage

Protein crystallization demands the fundamental understanding of nucleation and applying techniques to find the optimal conditions to achieve the kinetic pathway for a large and defect free crystal. Classical nucleation theory predicts that the nucleation occurs at high supersaturation conditions.In this dissertation we sought out to develop techniques to attain optimal supersaturation profile to a large defect free crystal and subject it to *in-situ* X-ray diffraction using microfluidics. We have developed an emulsion-based serial crystallographic technology in nanolitre-sized droplets of protein solution encapsulated in to nucleate one crystal per drop. Diffraction data are measured, one crystal at a time, from a series of room temperature crystals stored on an X-ray semi-transparent microfluidic chip, and a 93% complete data set is obtained by merging single diffraction frames taken from different un-oriented crystals. As proof of concept, the structure of Glucose Isomerase was solved to 2.1 Å. We have developed a suite of X-ray semi-transparent micrfluidic devices which enables; controlled evaporation as a method of increasing supersaturation and manipulating the phase space of proteins and small molecules. We exploited the inherently high water permeability of the thin X-ray semi-transparent devices as a mean of increasing the supersaturation by controlling the evaporation. We fabricated the X-ray semi-transparent version of the PhaseChip with a thin PDMS membrane by which the storage and the reservoir layers are separated, and studies the phase transition of amorphous $CaCO_3$.

Contents

List of Tables

List of Figures

Chapter 1

Introduction

"Structure determines function" is the mantra of structural biology. X-ray diffraction from protein crystals is the most prevalent method of determining protein structure; therefore crystallizing protein is a critical step in the structure pipeline. It also has important applications in drug delivery [15, 44] and large-scale protein purification [43, 97]. Identifying effective crystallization conditions can be a major obstacle in all of these applications. The structure pipeline consists of screening a protein against a wide range of precipitants. In the case that crystallization occurs, crystals are cryo-cooled to minimize radiation damage and mounted in a x-ray beam. Crystals are selected to be large enough to provide diffraction from many different crystal orientations in order to collect enough information to solve the structure. This standard method is challenging when the crystals are small and fragile as thermal stresses induced during cryo-cooling damages the crystals, which in turn degrades the quality of the diffraction data. Fabricating a microfluidic platform that allows growing protein crystals using well controlled crystallization conditions combined with in-situ x-ray diffraction data collection eliminates the above mentioned challenges.

Nucleation is a stochastic, non-equilibrium, dynamic process that in proteins occurs on

the nanometer scale, which requires high supersaturation. Despite the lack of experimental details about nucleation, classical nucleation theory [46, 47, 48, 95] formulates the kinetics of nucleation. The total change in free energy in creating an embryo or a nucleus from bulk phase is given by,

$$\Delta G = \Delta G_v + \Delta G_s \tag{1.1}$$

Where $\Delta G_v = -\frac{4\pi r^3}{3V}\Delta\mu$ is the volume energy and $\Delta G_s = 4\pi r^2\gamma$ is the surface energy of a spherical cluster of radius r. V is the molecular volume, $\Delta\mu$ is the difference in chemical potential between solution phase and crystalline phase and γ is the interfacial tension between the solid phase and the bulk solution phase. There is an energy barrier ΔG^*, due to competition between volume and surface free energies of the solid phase, shown in Figure 1.1.

$$\Delta G = -\frac{4\pi r^3}{3V}\Delta\mu + 4\pi r^2\gamma \tag{1.2}$$

The activation energy is

$$\Delta G^* = \frac{16\pi}{3}\frac{V^2\gamma^3}{\Delta\mu^2}$$

where, r^* is the radius of the critical nucleus.

The nucleation rate is proportional to the Boltzmann weight associated with the activation energy and is given by,

$$J \propto e^{-\frac{\Delta G^*}{k_B T}} \tag{1.3}$$

In heterogeneous nucleation because of the presence of a surface of lower energy for the protein, the effective surface tension is reduced, but a barrier still remains.

For protein nucleation and crystallization studies we used Glucose isomerase at the majority of the time. Glucose Isomerase (also known as D-xylose isomerase) is an enzyme that catalyzes the interconversion of D-xylose and D-xylulose. It's a 173 kD protein with or-

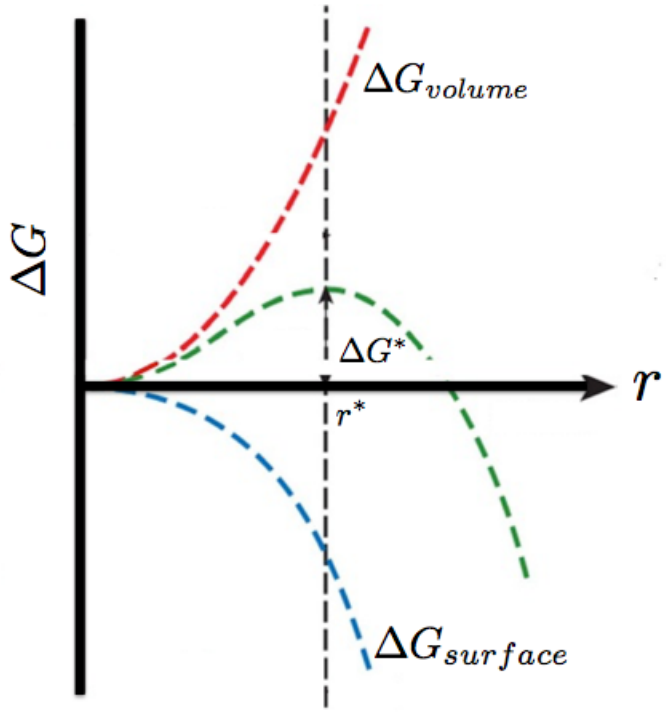

Figure 1.1: Energy barrier, ΔG^*, for nucleation which is a result of competition between volume free energy, ΔG_v and surface free energy, ΔG_s.

thorhombic symmetry in the space group I222 and exhibits a TIM barrel fold and a tetrameric quaternary structure as can be seen in Figure 1.2. The structure of D-xylose isomerase is (from *streptomyces rubiginosus*) has been determined using X-ray diffraction and refined up to 1.9 Å resolution [12]. We've used Glucose Isomerase from *Streptomyces rubiginosus* (from Hampton Research) and at a later time we purified and and crystallized Glucose Isomerase from *Thermus thermophilus*. The purification and crystallization steps are listed in Appendix 3.

With the use of microfluidics techniques we also set out to understand the crystallization of the small molecules such as biominerals. Calcium carbonate is vastly studied, abundant biomolecule which still acquires a great amount of interest among the biomaterials commu-

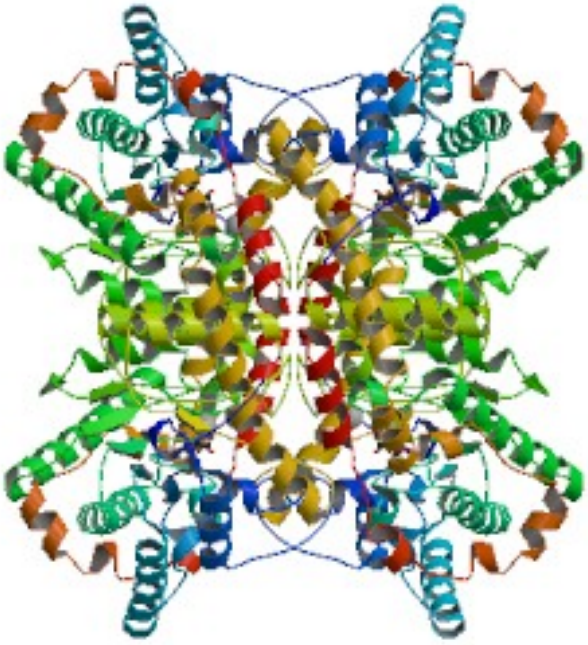

Figure 1.2: D-Xylose isomerase tetramer from

nity. We are interested in investigating the formation of Calcium carbonate and its precursor in the amorphous phase.

The main goal of this Dissertation is to develop microfluidics technique to grow protein crystals using well controlled crystallization conditions combined with in-situ x-ray diffraction data collection. Chapter 2 describes the X-ray semi-transparent microfluidics technology and it's use on room temperature *in-situ* X-ray diffraction in kinetically optimized emulsion drops of protein. Chapter 3 presents study carried out to crystalize proteins in the X-ray semi-transparent microfluidics devices via controlled evaporation, exploting the inherent property of high water permeability of these devices. Chapter 4 reports the design and fabrication details of the fix target support wafers and grids as a sample delivery sysytem, to facilitate X-ray free electron lasers. Chapter 5 describes the X-ray semi transparent version of the PhaseChip fabricated for the first time, along with the X-ray scattering experiments

carried out on theCalcium Carbonate system. Finally, Chapter 6 concludes this Dissertation with a short description on the future of the X-ray semi transparent microfluidic technologies described here.

Chapter 2

Room-temperature serial crystallography using a kinetically optimized microfluidic device for protein crystallization and on-chip X-ray diffraction

This chapter is adapted from [39]which is originally published in *IUCrJ*.

Abstract

We developed an emulsion based serial crystallographic technology in which nanoliter sized droplets of protein solution are encapsulated in oil and stabilized by surfactant. Once the first crystal in a drop is nucleated, the small volume generates a negative feedback mechanism

that lowers the supersaturation, which we exploit to produce one crystal per drop. We diffract, one crystal at a time, from a series of room temperature crystals stored on an X-ray semi-transparent microfluidic chip and obtain a 93% complete data set by merging single diffraction frames taken from different unoriented crystals. As proof-of-concept we solved the structure of glucose isomerase to 2.1 angstrom, demonstrating the feasibility of high-throughput serial X-ray crystallography using synchrotron radiation.

2.1 Introduction

In conventional protein X-ray crystallography, a complete data set is ideally obtained from a single crystal, which typically requires a relatively large crystal that has been successfully cryocooled. Serial crystallography takes the opposite approach: complete diffraction sets are assembled from a large number of individual diffraction frames acquired from small, single, unoriented crystals that are not cryoprotected [35, 87, 13, 10]. Complete coverage of the Ewald sphere is obtained by assembling individual diffraction frames into a single data set. The ideal crystals for serial crystallography are large enough and sufficiently defect free to diffract to high resolution, are produced in large quantity, and are sufficiently identical to facilitate merging of diffraction frames.

Serial crystallography with non-cryocooled crystals has several technical advantages over conventional methods. First, the crystals can be small, which increases the potential for growing crystals in the first place. Second, it avoids the roughly ten-fold increase in crystal mosaicity typically encountered during cryoprotection [58, 35] and eliminates the need to search for cryoprotectant conditions. Although non-cryoprotected crystals suffer radiation damage at a roughly hundred times higher rate than cryoprotected crystals [30], there is little disadvantage associated with using many non-cryocooled crystals to obtain a complete

data set if the crystals are easy to produce, plentiful, and easy to handle.

The ideal crystallization procedure, illustrated in Figure 2.1A, to produce protein crystals for any form of crystallography, including serial crystallography, consists of slowly increasing the supersaturation of a protein solution until the moment that a single crystal is nucleated. Then, once the first nucleation event occurs, the supersaturation is reduced enough to prevent further nucleation, while remaining supersaturated enough to grow the crystal. Ideally, the growth conditions should be slow enough to allow for annealing of defects, and the procedure must be capable of producing crystals in large numbers and of identical size. Additionally, the technology to produce crystals must be simple and inexpensive if serial crystallography is to become adopted by the structural biology community.

The challenge is to design such a method. The well known Counter-Diffusion method [29, 28, 66] produces a series of kinetic supersaturation profiles that rise and fall as illustrated in Figure 2.1A. However, both the time at which the supersaturation maximum occurs and the value of the supersaturation maximum are independent of the nucleation event. The maximum supersaturation varies along the capillary length and with a long capillary the chances are improved that somewhere along the capillary there will be a location where the maximum supersaturation will coincide with the first nucleation event. However, this method requires long capillaries and is not optimal for volumes under 1 nl. Furthermore, Counter-Diffusion requires that the precipitant and protein have greatly different diffusion constants, so it is suitable for low molecular weight precipitants, such as salt, but not for macromolecules, such as poly(ethylene glycol) (PEG).

Another issue complicating design of the ideal profile of Figure 2.1A, is that at constant supersaturation nucleation is a random process, rendering it impossible to *a priori* know when to decrease supersaturation, which should coincide with the first nucleation event. One way to generate the ideal supersaturation profile would be to monitor the supersaturated

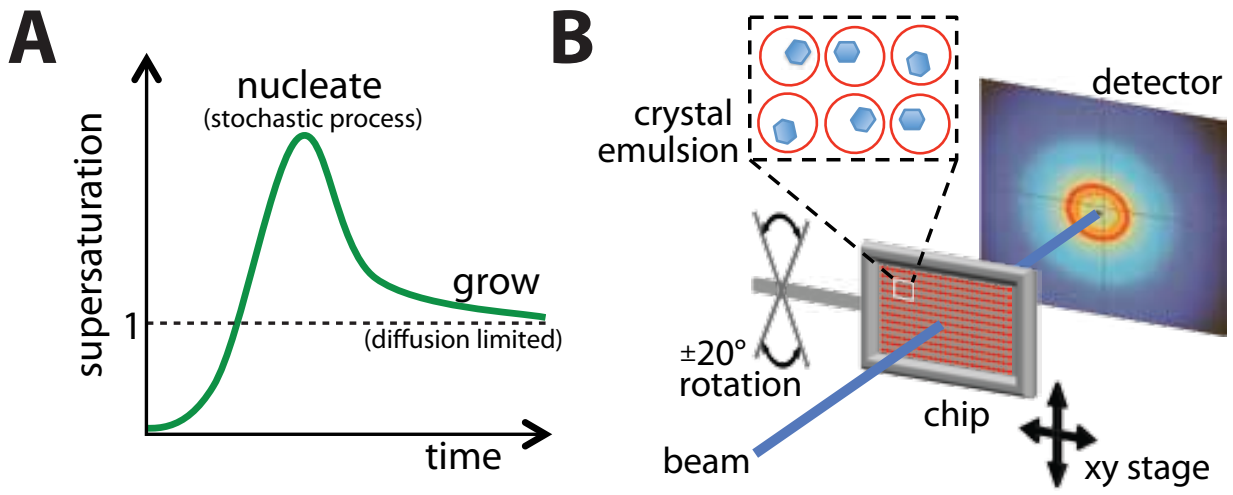

Figure 2.1: (A) An optimal crystallization trajectory increases supersaturation until just one crystal nucleates, then decreases supersaturation to prevent further nucleation, while remaining supersaturated enough to promote crystal growth. (B) Emulsion droplets with monodisperse crystals were stored in an X-ray semi-transparent microfluidic device. Sequentially collected diffraction frames from multiple individual crystals were merged to solve the protein structure. The chip could be translated in x- and y-directions and rotated ±20°.

solution with a technique, such as Second Harmonic Generation (SHG) microscopy [99, 50], that is sensitive to the formation of small crystals and then, once the first crystal is detected, lower the supersaturation. However, this scheme will be cumbersome to implement in the high throughput case of processing hundreds to thousands of samples. An alternative method is desired.

Microfluidically produced, monodisperse, emulsions have previously been used to produce drops of supersaturated protein solution in which each drop nucleates a single crystal [105, 42, 81, 18]. This situation is ideal for serial crystallography for a number of reasons. Since only one crystal nucleates per drop, all the supersaturated protein in solution is delivered to a single crystal, making that crystal as large as possible. Microfluidic precision allows preparation of emulsion droplets with variations in size of a few percent only, even at high flow rates [74]. Furthermore, because of the small length scales in microfluidics, convection

is suppressed and flows are laminar. Taken together, processing proteins using microfluidics leads to crystals of the uniform size that are grown under identical conditions, which has the effect of creating crystals that have similar characteristics, such as unit cell and degree of disorder. Having identical crystals facilitates merging of diffraction data sets taken from different crystals.

In the microfluidic device described here, we first produce drops containing protein. Then, exploiting surface tension forces, we guide drops to 8,000 storage sites on-chip [84, 79]. Next, we increase supersaturation to induce crystallization in such a way as to produce one crystal per drop. Finally, we sequentially collect diffraction from individual crystals and merge data sets in order to solve the protein structure (Figure 2.1B).

Producing and diffracting from crystals in the same device eliminates the laborious and potentially damaging steps of looping and extracting the crystal from the mother liquor. Various microfluidic crystallization platforms compatible with *in situ* diffraction have been developed [36, 52, 17, 35]. However, these devices incorporated valves in the chip [36, 35], thus rendering them expensive to manufacture and difficult to operate. Other technologies are low-throughput [17], or need a second round of scale-up to larger capillaries [52] to produce crystals large enough to collect diffraction data.

2.2 One crystal per drop through compartmentalization

The production of one crystal per drop is a result of a competition between two processes, nucleation and growth, in a confined volume. Both processes require supersaturation and therefore both nucleation and growth are nonequilibrium processes. When the first nucleus

forms inside the drop, it decreases the supersaturation in the surrounding protein solution as the crystal grows. If the rate of nucleation is low enough, then the growing crystal will consume enough of the protein in solution to decrease the supersaturation to the point where another nucleation event is improbable. Further nucleation is prevented if the time for a protein to diffuse across a drop is less than the time to nucleate a crystal [18]. Thus combining a small drop volume with the physics of nucleation and growth, generates negative feedback that acts to autonomously create the ideal dynamical supersaturation profile that produces one crystal per drop. Instead of having the negative feedback imposed externally, as in the cumbersome Second Harmonic Generation microscopy scheme discussed previously, here the negative feedback is engineered into each drop; no external intervention is required. All the engineering goes into identifying the correct combination of diffusive flux, nucleation rate and drop volume for the emulsions. A theoretical argument and computer simulations describing the processes leading to one crystal per drop in small volumes is detailed in the Appendix.

2.3 Crystal emulsions

To yield identical crystals in sufficient quality and quantity for serial crystallography, we use a two step method. We first identify the appropriate drop volume to consistently nucleate one crystal per drop. For this we intentionally created emulsions in a batch process that yielded a polydisperse size distribution, ranging from a few micrometers to a few hundreds of micrometers in diameter (Figure 2.2A-C). Such a polydisperse emulsion allowed us to identify the appropriate drop diameter in a single screening experiment. We then used microfluidics (Figure 2.2D) to produce monodisperse emulsion droplets (Figure 2.2E-F), which we used to grow identical crystals in the serial X-ray diffraction chip, as described in Section 5. For

Table 2.1: Properties of crystallized proteins. The theoretical pI value of D1D2 was computed using its amino acid sequence and the ExPASy ProtParam tool [69].

	formula weight	**isoelectric point (pI)**	**net charge in crystal**
Lysozyme	14.3 kDa	11.3 (from [103])	positive
Trypsin	24 kDa	10.1 - 10.5 (from [98])	positive
Concanavalin A	76.5 kDa (3mer)	4.5 - 5.5 (multiple isoforms, see [21])	negative
Glucose isomerase	173 kDa (4mer)	3.95 (from [96])	negative
D1D2	26.8 kDa (heterodimer)	10.6 (theoretical pI, from [69])	positive

the purposes of this paper, however, the full experimental sequence will only be reported for glucose isomerase, i.e, whereby crystals were grown in the serial diffraction chip, X-ray data were acquired, and the structure was solved.

All crystals were grown in emulsion droplets stabilized against coalescence with a 2% v/v solution of PFPE-PEG-PFPE surfactant "E2K0660" in HFE7500 fluorinated oil (from 3M). The surfactant was synthesized as previously described [40]. Note that a commercial surfactant, which we have used in other experiments, is now available [70]. We chose a fluorinated oil and surfactant to minimize interactions with biological molecules. Fluorocarbon and hydrocarbon oils do not mix with each other, nor do they mix with water. In particular, the PFPE-PEG-PFPE surfactant in HFE7500 oil system has been shown to have excellent bio-compatibility [40, 76]. To confirm that it is compatible with protein crystallization, we tested it with five crystallization model proteins (Figure 2.2 and Table 2.1). All five model proteins have previously been crystallized by vapor diffusion and a structure derived from X-ray crystallography deposited in the PDB.

To adopt a published vapor diffusion recipe into our emulsion format we had to perform a set of pre-experiments. In traditional vapor diffusion, a small volume of protein solution is mixed with the same amount of precipitant and then sealed into a container together with a

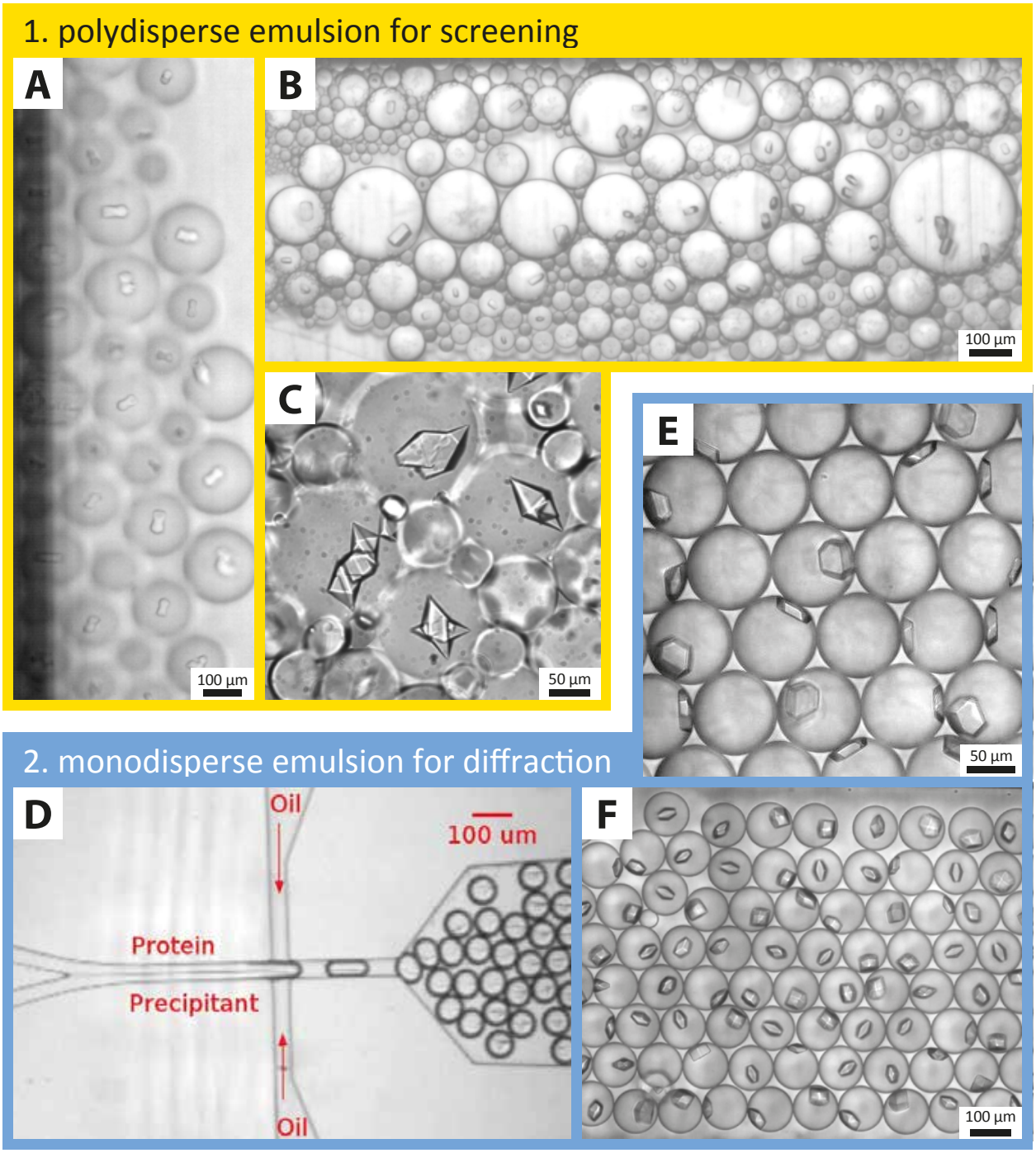

Figure 2.2: Protein crystallization in emulsion droplets stabilized by surfactant. Ideal drop sizes were first identified using polydisperse emulsion droplets. Monodisperse emulsion were used to produce identical crystals for diffraction experiments. Droplets were stored in a rectangular glass capillary. (A to C) Polydisperse emulsions of (A) D1D2 heterodimer from human spliceosomal snRNP particle, (B) concanavelin A, and (C) trypsin. (D) Protein and precipitant solutions were introduced in a co-flow geometry under laminar flow conditions that prevent mixing upstream of the nozzle where both solutions became encapsulated into emulsion droplets. (E and F) Monodisperse emulsions of (E) glucose isomerase and (F) lysozyme crystals. See main text for crystallization conditions. (D and F) from[4].

large reservoir of precipitant. The diluted protein-precipitant drop equilibrates through vapor phase diffusion with the reservoir, resulting in a concentration increase of all components in the drop by approximately a factor of two. All previously published crystallization recipes had been optimized to nucleate only a few crystals per microliter. Our emulsion droplets have volumes of a few pico- to nanoliter each. As the probability of nucleating a crystal is proportional to the sample volume, we had to increase nucleation rates by at least two orders of magnitude. We thus prepared vapor phase and microbatch crystallization trials around the literature recipes and optimized the vapor recipes toward nucleating crystal showers of appropriate density. When attempting to crystallize a novel protein target through screening crystallization conditions such crystal showers are usually considered a first hit and the conditions are later refined extensively to grow the largest possible crystal. When using the method presented here on a novel protein target, the polydisperse emulsion screen can directly be used with conditions giving crystallites and crystal showers commonly identified as first hits in vapor diffusion screens. This would eliminate the reverse engineering step of converting an optimized vapor phase recipe back to a recipe that grows crystal showers.

Polydisperse emulsions were then prepared by mixing 2 μL protein solution with 2 μL precipitant in a 150 μL PCR test-tube. Immediately after mixing, we added 30 μL 2% v/v solution of PFPE-PEG-PFPE surfactant (E2K0660) in HFE7500 fluorinated oil. Polydisperse emulsions were formed by gently agitating the vial by hand until droplets became too small to be resolved by eye. This procedure typically gave droplets ranging from a few micrometers to a few hundreds of micrometers in diameter (Figure 2.2A-C). Aqueous droplets were less dense then the immersing fluorinated oil, so droplets rose ("creamed") to the top of the vial within a minute. The emulsion cream was then loaded into rectangular glass capillaries (VitroTubes from VitroCom, Mountain Lakes, NJ, USA) and sealed with 5 minute Epoxy to prevent evaporation. Crystallization was monitored over the course of a week.

All compounds and proteins from commercial sources were used as received without further purification. The molecular weight and the net charge of the proteins during crystallization, as derived by the isolectric point, are summarized in Table 2.1. To first order, preparing a polydisperse emulsion takes about the same time as preparing a hanging or sitting drop vapor diffusion condition. Both require three pipetting steps and a final lidding or shaking operation. We also successfully used conventional pipetting robots and 96 well plates for emulsion screening.

Lysozyme was crystallized by encapsulating 30 mg/ml Lysozyme, 100 mM sodium acetate, pH 4.8, 12.5 wt% PEG 8000, 5 wt% NaCl (all Sigma Aldrich) final concentration into droplets and then incubating them at 6°C for 36 hrs until all droplets had nucleated crystals [4]. This recipe was derived from a vapor phase recipe mixing 20 mg/ml lysozyme in 100 mM sodium acetate pH 4.8 with an equal volume 10% (w/v) NaCl, 100 mM sodium acetate pH 4.8, and 25% (v/v) ethylene glycol [73].

Glucose isomerase crystals were grown at room temperature (∼25°C) within two days by preparing a crystallization batch with final concentrations of 30 mg/ml glucose isomerase from *Streptomyces rubiginosus* (from Hampton Research), 100 mM ammonium sulfate, pH 7.0, 20 wt% PEG 10,000 in a 1 : 1 ratio (all from Sigma Aldrich). The initial vapor phase crystallization condition was taken from the Hampton Research data sheet as mixing 20 - 30 mg/ml glucose isomerase with 10 to 15% (w/v) PEG 4000 - 8000, 200 mM salt, pH 6.0 - 9.0.

Trypsin was crystallized by mixing 60 mg/ml trypsin (Sigma T-8253) from bovine pancreas in 10 mg/ml benzamidine, 3 mM $CaCl_2$, 0.02 wt% sodium azide with 100 mM $NaPO_4$, pH 5.9, 5.1 M ammonium acetate (all Sigma Aldrich). In this system we observed crystals within one day in the range of pH 5.9 to pH 8.6, with higher pH values having much higher nucleation rates. This recipe was derived from a vapor phase recipe mixing 60 mg/ml trypsin

in 10 mg/ml benzamidine, 3 mM calcium chloride, and 0.02% (w/v) sodium azide with an equal volume of 4% (w/v) PEG 4000, 200 mM lithium sulphate, 100 mM MES pH 6.5, and 15% ethylene glycol [73].

Concanavalin A was crystallized by mixing 25 mg/ml concanavalin A type IV from *Canavalia ensiformis* in 10 mM tris hydrochloride, pH 7.4 with 100 mM tris hydrochloride, pH 8.5, 8 wt% PEG 8,000 in a 1 : 1 ratio (all from Sigma Aldrich). For this we first set-up vapor phase and microbatch trials of 20 mg/ml Concanavalin A in 10 mM TRIS pH 7.4 against the 50 conditions in the Hampton Crystal Screening Kit. From this screen we choose condition 36, with 100 mM tris hydrochloride, pH 8.5, 8 (w/v) PEG 8000, as this condition grew crystals in both vapor phase and microbatch trials.

D1D2, the sub-complex from the human snRNP spliceosome core particle (PDB entry 1B34 [45]), crystallized over 72 hrs at room temperature by preparing a crystallization batch with final concentrations of 6 mg/ml D1D2, 62 mM sodium citrate pH 5.2, 125 mM ammonium acetate, 9 vol% glycerol, 26 wt/vol PEG 4,000 (all Sigma Aldrich). D1D2 was purified as previously reported [45]. D1D2 was first crystallized by Kambach et al. [45] in vapor phase by mixing equal volumes of 6 mg/ml D1D2 in 20 mM sodium HEPES pH 7.5, 200 mM sodium chloride and 6 mM dithiothreitol and 100 mM sodium citrate pH 5.6, 200 mM ammonium acetate, 15% glycerol, 25% PEG 4000. All globular proteins, concanavalin, glucose isomerase and trypsin, crystallized readily in vapor diffusion, microbatch, and the emulsion system. The heterodimer D1D2 formed crystals in vapor phase and the emulsion system only. In microbatch a thick protein skin grew at the droplet interphase potentially depleting all the protein from the drop. We thus conclude that the PFPE-PEG-PFPE surfactant system is well suited to protect protein from absorbing to the fluorooil-water interface and to stabilize emulsions, making it ideal for crystallization trials. Future work should investigate compatibility of the surfactant with other proteins. In particular, in membrane

protein crystallization, detergents are part of the crystallization cocktail, which may interact with the PFPE-PEG-PFPE surfactant. However, the two membrane proteins porin from *R. capsulatus* and reaction center from *R. viridis* have previously been crystallized in a related fluorinated FC-40 and FC-70 oil [52].

All initial crystallization experiments were performed at room temperature. However, a particular protein may become unstable at too high or too low temperatures. Also, many proteins like lysozyme have temperature sensitive nucleation rates, which one might like to exploit in crystallization trials [4]. An ideal surfactant-oil system can hence be used in a large temperature range. To test for temperature compatibility, we prepared crystal emulsions from the PFPE-PEG-PFPE surfactant in HFE7500 oil, sealed them into rectangular glass capillaries and incubated them in a water bath at 4°C and at 40°C. We found the emulsion droplets to be stable for at least two weeks at those two temperatures.

Finally, to yield identical crystals in sufficient quantity for serial crystallography, we employed microfluidics to produce monodisperse emulsion droplets. For this we simply selected the dropmaking chip appropriate to make drops of the desired diameter and used the crystallization recipe from the preceding polydisperse emulsion screen without further modification. We produced drops in a co-flow geometry designed such that the protein solution and buffer do not mix in the laminar flow upstream of the dropmaker (Figure 2.2D). Typically, injection of the oil-surfactant mixture proceeded at 600 μL/hr, while both protein and precipitant streams were pumped at equal flow rates of 300 μL/hr to co-encapsulate both in a 1:1 mixture. Upon droplet formation, mixing inside each droplet proceeds within less then a second due to recirculating flow that arises from shearing interactions of the fluid inside the drops with the stationary wall [93]. These monodisperse emulsion droplets were then injected into and incubated in the diffraction chip to grow crystals for the X-ray diffraction experiments.

To monitor crystallization, we stored emulsion droplets in two different systems. Firstly,

polydisperse emulsions were usually sealed into rectangular glass capillaries, which prevented water and oil evaporation. Secondly, as our diffraction chip was made from a polymer material, we exploited its permeability to water vapor by slowly letting droplets shrink by permeation of water from the drops into the oil and also from the drops through the thin, polymer-based chip. Water permeation across the polymer foil decreases linearly with increasing foil thickness and decreased permeability of the material [84]. In case of the 25 to 75 μm thick COC sheets used here, the evaporative water loss amounted to a few percent per hour. When water evaporates from the drop, the solute concentrations inside the drop increase and hence the protein supersaturation also increases. As this corresponds to an increased nucleation rate, one would expect to yield a larger fraction of droplets with multiple crystals. We did not observe such an effect and attribute this to the fact that once the first crystal nucleates, its subsequent growth reduces the supersaturation of the solution enough to prevent another crystal from nucleating. We consistently achieved one crystal per drop, which argues for the robustness of the method. Once all droplets had nucleated crystals after a few hours or days, we immersed the capillary/chip into an oil bath to prevent further evaporation [52]. Alternatively we achieved equally good results with storing chips in a water bath to which a vial filled with oil was connected to the chip and all other inlets were sealed.

2.4 X-ray semi-transparent chip fabrication

A detailed description of the fabrication of the microfluidic chips is given in [35]. An overview and modifications for in-situ x-ray diffraction follow: Chips were sealed, which is colloquially referred to in the thermoplastic industry as 'lidding', by bonding cyclic-olefine-copolymer (COC)- or Kapton-foil to both sides of the thin poly(dimethylsiloxane) (PDMS) slab con-

taining the channels (Figure 2.3). PDMS (Sylgard® 184 from Dow Corning) with ratio 1:5 of curing agent to base was molded on a standard SU8-master [61] by squeezing the uncured PDMS resin into a thin film using a glass plate and a weight. To facilitate release of the PDMS film the master was surface treated with a fluorophilic coating by spin-coating 1:20 Cytop CTL-809M in CTsolv.100E (both Bellex International) onto the master. We then baked the wafer for 1 hr at 150°C. We placed a 30 μm thick Mylar foil (DuPont) between PDMS and glass to allow for easy removal of the glass slide after PDMS curing. We pre-cured the PDMS for 4 hr at room temperature before we removed the weight and transferred the complete stack into the oven to drive the curing reaction to completion at 72°C for another hour.

We either used COC (TOPAS® 5013 from Advanced Polymers) or Kapton (American Durafilm), depending on experimental requirements. COC is more brittle then Kapton, but has a lower water vapor permeability. The thinnest commercial COC we used was 25 μm thin TOPAS®, while Kapton as thin as 8 μm can be purchased as bulk foil. We chemically bonded either substrate to the featured PDMS using a silane coupling chemistry [89]. In brief, both foil and PDMS are activated in an oxygen plasma and then incubated for 25 minutes in an aqueous solution of a different silane each; 1 vol% of 3-aminopropyltrimethoxysilane (APTMS, 97% from Aldrich), and 1 vol% of 3-glycidoxypropyltrimethoxysilane (GPTMS, 98%, from Aldrich). The two silanes are such that they can form an epoxy bond when brought in contact. Upon removing foil and PDMS from the batch, we dried both with a stream of nitrogen gas and then carefully brought them in contact using tweezers to prevent trapping air bubbles between both layers. The chip was then incubated in the oven at 72°C for 1 hr to maximize chemical cross-linking. The process was repeated to lid the other side of the chip, now with a foil that had through at the appropriate locations for fluid-interfacing. Through holes were punched using a 0.75 mm Harrison Uni-Core biopsy

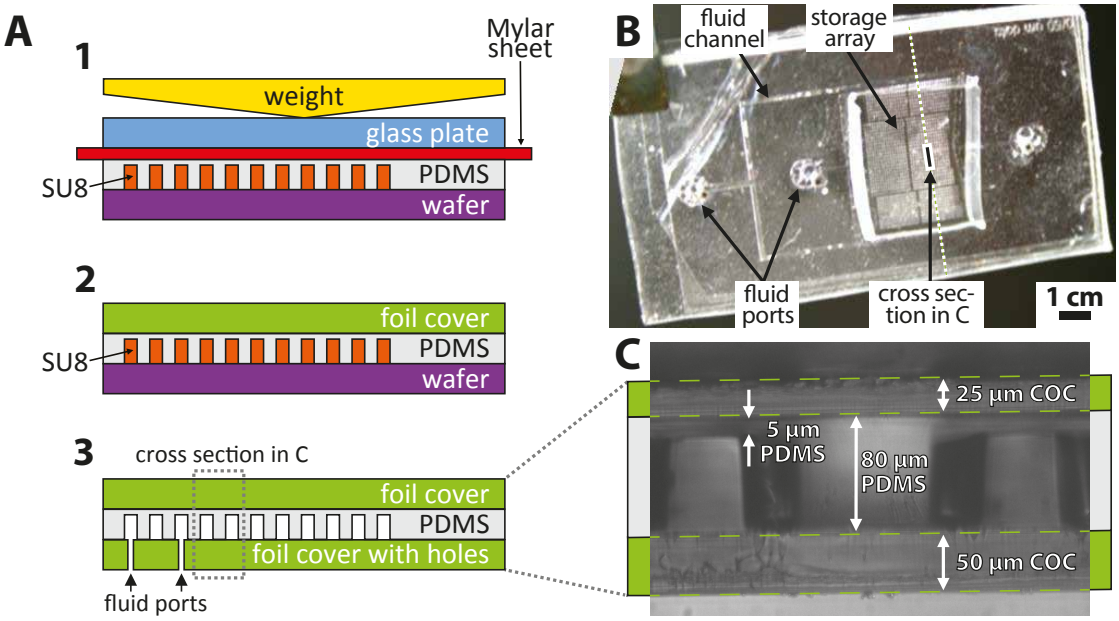

Figure 2.3: Chip fabrication. (A) PDMS resin was squeezed into a thin layer onto the SU8-master (1). After curing, a foil cover was bonded onto the featured PDMS using a silane coupling-chemistry [89] (2). Then the reinforced PDMS film was peeled off and the chip was lidded using another foil cover (3). (B) Top view and (C) cross-section of a device made from COC-foil and PDMS. The cross-section in (C) was imaged by cutting the chip across the storage array into two and was imaged by placing the chip edge on onto the microscope stage to magnify the cut. The chip shown here, had a 5 mm thick PDMS frame manifold for fluid interfacing where tubing could be directly inserted into the through holes in the PDMS.

punches (Ted Pella). Upon assembly the chip was surface treated with a fluorophilic coating to prevent protein interaction with the channel surface. For this, 1:20 Cytop CTX-109AE in CTsolv.100E (both Bellex International) was dead-end filled into the chip by plugging all outlets and slowly injecting the Cytop solution through the inlet into the chip. This causes gas bubbles trapped inside the chip to become pressurized which promotes the gas to dissolve into solution and also to permeate across the chip walls to result in a completely filled, bubble free device. The chip was then incubated at 90°C for at least 12 hrs to evaporate the solvent away and also to accelerate chemical cross-linking between fluoropolymer and chip surface.

2.5 *In-situ* diffraction

We mounted the X-ray transparent chip into a custom acrylic frame to collect diffraction data (Figure 2.4). The acrylic frame was cut to shape from 3 mm thick acrylic sheet using a 40 W CO_2 Hobby Laser cutter with a 1.5" focus lens (Full Spectrum Laser). To create ports into the foil-chip we drilled through holes into the acrylic frame with the laser cutter. Blunt needle tips (23 gauge) were then placed into the holes and glued into position with 5 minute Epoxy. We connected #30 AWG poly(tetrafluoroethylene) (PTFE) tubing (Cole Palmer) to the needle tips using PDMS cubes with through holes punched into them using 0.75 mm Harrison Uni-Core biopsy punches (Ted Pella). Buna O-rings, 70 durometer, size 002 (McMaster Carr) were then used to seal the foil-chip to the hollow metal pins. For easy alignment the o-rings were fit into a 1 mm thick poly(ethyleneterephthalate) (PET) spacer that also was fabricated with the laser cutter. X-ray semi-transparent foil-chips were mounted into a frame for the duration of each experiment. Each frame was held together by 10 self-tapping 3/16" Pan Head 2-28 Phillips screws (McMaster Carr) to lock the chip into position and to minimize flow induced inside the chip from mechanically bending the thin foil chip. To mount the frame-chip assembly in the synchrotron we machined a stainless steel adapter that a frame could be mounted onto using two screws (Figure 2.4B).

For the proof of principle experiment we fabricated an X-ray semi-transparent chip with the "dropspot" geometry [79] that can hold up to 8000 emulsion droplets in cavities with 150 μm diameter each (Figure 2.3 B&C). The fluorinated oil has a density of 2 g/mL, while the water drops have a density of 1 g/mL. Thus there is a strong tendency for the drops to float to the top of the oil, or "cream". Surface tension forces arrest droplets in a cavity and prevent them from creaming to one side of the chip. We produced a monodisperse $\sim$110 μm diameter emulsion of 30 mg/ml glucose isomerase, 100 mM Ammonium Sulfate,

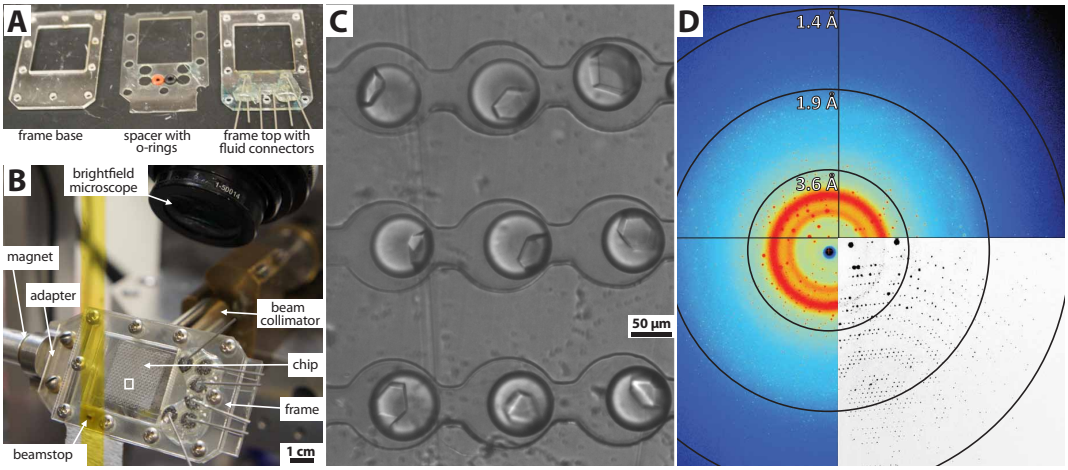

Figure 2.4: (A) Monodisperse emulsion were prepared using a dedicated dropmaking chip as illustrated in Figure 2.2D and directly routed into the chip for serial crystallography for storage. (B) We used a laser-cut frame to hold and to port into the X-ray semi-transparent chip. (C) X-ray semi-transparent chip mounted on the goniometer inside the Cornell CHESS F1 beamline. (D) Glucose isomerase crystals inside of the microfluidic device. Using a motorized stage, each crystal can be centered in the collimated X-ray beam. The beam is 100 μm in diameter. (E) Representative diffraction pattern of a glucose isomerase crystal taken at room temperature from inside the chip. Crystals diffracted to 1.4 Å resolution with a mosaicity as low as 0.04°. The bottom right quadrant shows the diffraction pattern after background subtraction, using the Adxv diffraction pattern visualization tool [3] with subtract background option.

pH 7.3, 20 wt% PEG 10k MW final concentration in a standard dropmaker (Figure 2.2D). Droplets exiting the dropmaker were immediately routed into the X-ray semi-transparent serial crystallography chip by simply plumbing the dropmaker outlet into the dropspot inlet (Figure 2.4A). After the dropspot chip was loaded, we dead-end plugged its outlet except for one inlet where we kept HFE7500 oil entering the chip using hydrostatic pressure to compensate for oil evaporation from the chip. We incubated the chip at room temperature for three days and monitored crystallization, before transferring into a water bath to prevent further evaporation. By then, most droplets had shrunken to about ~90 μm diameter and more than 90% of them had nucleated a single crystal. Crystals grew to about 50 μm by 40

Table 2.2: Processing results of merging the 248 frames obtained from 72 glucose isomerase crystals. Values in parentheses refer to the highest resolution bin (2.15-2.09 Å).

Precipitant composition	100 mM ammonium sulfate pH 7.0 + 20 wt% PEG 10,000
Space Group	I222
Unit-cell parameters (Å)	$a = 93.94$ $b = 99.47$, $c = 102.85$
Resolution range (Å)	49.7 - 2.09 (2.15 - 2.09)
No. of unique reflections	26699 (2075)
Redundancy	8.2 (8.1)
Completeness (%)	93.2 (94)
R_{merge} (%)	0.191 (0.686)
$< I/\sigma(I) >$	7.8 (4.1)
Mosaicity (°)	0.03-0.1

μm by 30 μm in size at room temperature ($\sim$25°C)

X-ray diffraction data were collected at Cornell High Energy Synchrotron Source (CHESS), beamline F1 ($\lambda = 0.9179$ Å, $E = 13.508$ keV, X-ray flux = 5.53 * 10^{10} photons/sec), using a 100 μm monochromatic X-ray beam from a 24-pole wiggler. The chips were mounted at a distance of 200 mm from an Area Detector Systems Corporation (ADSC) Quantum 270 (Q270) detector, corresponding to a largest inscribed circle of resolution of 1.4 Å. The detector face was oriented perpendicular to the beam. For selected crystals within the chip, data sets were collected at room temperature ($\sim$25°C). Each recorded data set comprised 10 frames, for a total of 10° oscillation. Each image consisted of a 5 second exposure with a 1° oscillation step size. A total of 1520 images were collected from 152 glucose isomerase crystals in three different dropspot chips.

2.6 X-ray structure determination

The software HKL-2000 was used to index, refine, integrate and scale each 10° data set [67] before merging. Parameters including unit-cell size, chi-squared values, resolution, mosaicity,

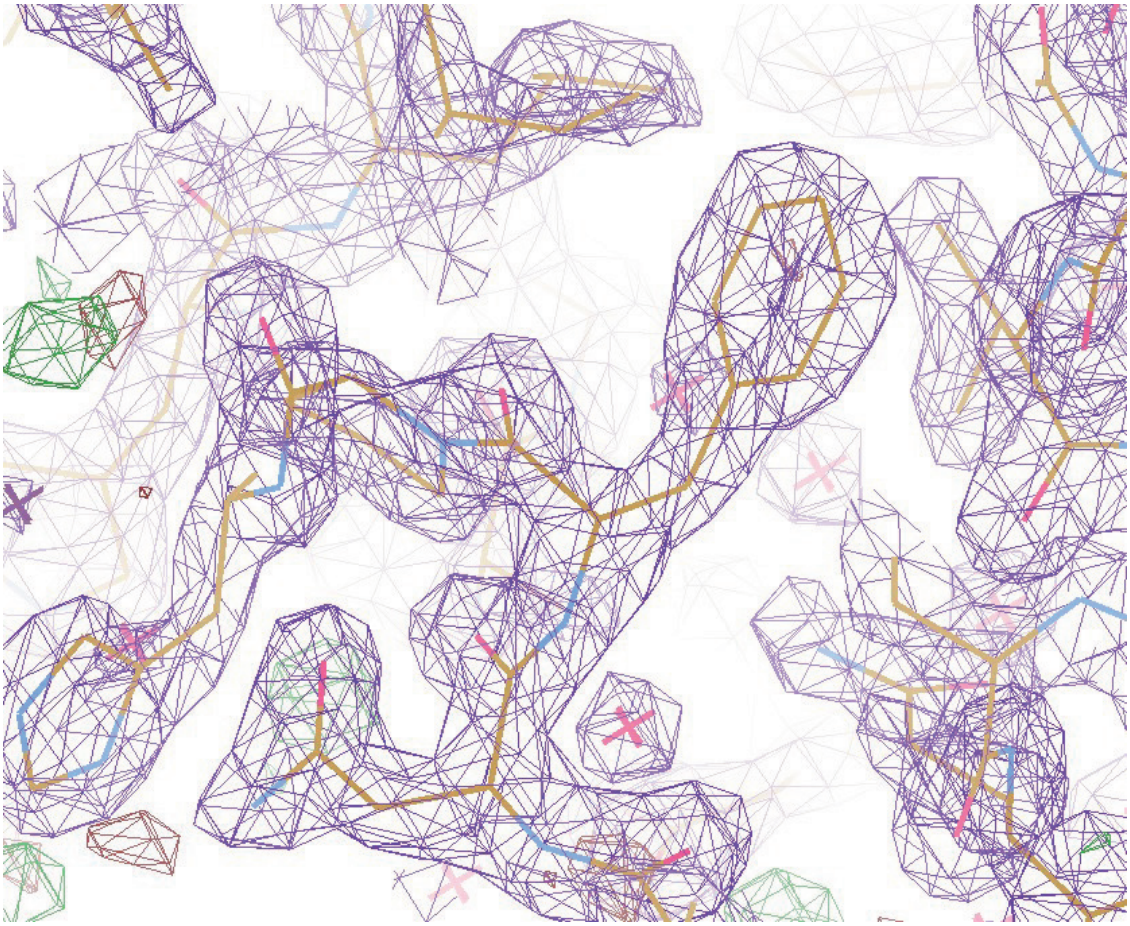

Figure 2.5: Part of the final structure of Glucose Isomerase refined to 2.09 Å showing the quality of the electron density map. The limiting resolution of 2.09 Å was chosen as that at which CC1/2 dropped below 0.5. 2Fo-Fc map is in magenta, contoured at 2 σ, Fo-Fc in red (negative) and green (positive), contoured at 3 σ.

and completeness were evaluated for every partial data set during the indexing and scaling process. From these partial data sets, with 1520 frames total, we selected 262 frames from 72 crystals by rejecting frames with a mosaic spread higher than 0.1° and chi-squared x and y (corresponding to discrepancy between observed and predicted spot positions) above 2. Some frames were later rejected because of poor scaling statistics; the final data set included 248 frames.

Glucose isomerase crystals were determined to have a space group of $I222$, and diffracted to an average of 2 Å; an example image is shown in Figure 2.4E. In some crystals, diffraction extended to 1.4 Å, with a mosaic spread of 0.04.

The 248 selected frames were scaled together using Scalepack (HKL Research) and merged with Aimless [22]. The limiting resolution of 2.09 Å was chosen as that at which CC1/2 dropped below 0.5. Statistics are given in Table 2.2. The merged data set covered 93% of reciprocal space, suggesting that preferred orientation of the crystals was not a major problem. The glucose isomerase structure was readily solved by molecular replacement with Molrep [94] using the structure previously determined at 1.90 Å resolution (PDB ID: 8XIA) [12], with waters removed. Prior to refinement, we randomly flagged 5% of the reflections for R_{free} analysis [11].

Structure refinement was carried out through multiple iterations of Refmac [63], refining atomic coordinates and isotropic B-factors. 2Fo-Fc and Fo-Fc electron density maps were generated after each refinement step, and further refinement was carried out by manual inspection using Coot [20]. In the refinement process, two disordered N-terminal residues were removed, as well as a bound sugar molecule present in the model but not in the crystal, and 124 water molecules were added. Final refinement gave R and R_{free} of 14.4% and 17.5%, respectively. Complete processing statistics are given in Table 2.3. Figure 2.5 shows the quality of the final refined structure.

2.7 Conclusion

Here, we present a technology that optimizes the kinetics of crystallization, eliminates crystal handling, eliminates cryoprotection and simplifies collection of diffraction data for structural biology. In this paper we developed processing methods for protein crystallization that follow

Table 2.3: Refinement and model statistics for glucose isomerase. Values in parentheses refer to the highest resolution bin.

Resolution range (Å)	49.7 - 2.09 (2.14 - 2.09)
Reflections used: working, total	25395, 26685 (1879, 1974)
Completeness (%)	92.4 (93.6)
R(working)/ R_{free}	0.144/ 0.174 (0.186/ 0.227)
RMSD, bond lengths (Å)	0.019
RMSD, bond angles (°)	1.93
No. of protein/other atoms (non-hydrogen)	3034/ 126
Mean B value, all atoms ($Å^2$)	17.6
Ramachandran statistics (%); favored, allowed, outliers	97.13, 2.35, 0.52

R and R_{free} are calculated using $\Sigma|Fo| - |Fc|/\Sigma|Fo|$ for the working and free-set reflections, respectively.

the ideal kinetic pathway of slowly increasing supersaturation until a single crystal nucleates and then reducing supersaturation so that one crystal grows slowly to allow annealing of defects. Sample volume is not a thermodynamic variable in phase equilibrium, but since crystallization is a non-equilibrium process, volume plays a key role in determining the kinetics of crystallization. In the Appendix, we argued using a combination of simulation, theory and experiment that selecting the appropriate droplet diameter, w, guarantees that only one crystal per drop will form when the drop volume $V <\sim (D/J)^{\frac{d}{2+d}}$. We identify the critical drop diameter for a particular crystallization condition in a single experiment by using a polydisperse emulsion with droplets ranging from a few micrometers to a few hundreds of micrometers in size. These polydisperse emulsions can be made with ease within seconds using only a pipette and a test tube. The probability of crystallization is proportional to drop volume. As we use drops of order 1 nl, which are smaller drops than employed by other methods, the nucleation rates and supersaturation that we use are higher than usual. It remains to be seen how such high nucleation and growth rates impact crystal quality. In the future we will study the quality of protein crystal structure determination as a function

of crystal size, nucleation rate and crystal growth rate to determine the optimal crystal size and crystallization conditions for serial crystallography.

Employing these kinetic processing methods, we grew monodisperse crystals compartmentalized in emulsion droplets, with one crystal per drop. Monodisperse, microfluidically produced drops of supersaturated protein solutions were stored on chip and slowly concentrated as water permeated through the thin foil chip. Single crystals per drop were nucleated and grown on-chip in identical conditions. While cyro-cooled crystals can be stored almost indefinitely, the crystals grown and stored in our chips are stable for several weeks when the chips are stored in a water bath connected to an oil reservoir, which prevents evaporation and hence drying out. The chip for nucleating crystals was thin enough to be X-ray semi-transparent and diffraction patterns were collected from these crystals on-chip at room temperature. The structure of glucose isomerase was solved and refined at 2.09 Å resolution, to an R_{cryst}/R_{free} of 0.144/0.174, using merged diffraction datasets from 72 crystals of about 50 μm by 40 μm by 30 μm in size.

Diffraction from room temperature crystals stored on the chip in which they were nucleated and grown has many advantages over traditional off-chip cyroprotected crystals. On-chip diffraction means the crystals are not removed from their mother liquor, which can lead to dehydration and osmotic shock of the crystals and the generation of stress and strain. Room temperature diffraction eliminates the laborious step of cryoprotection and has the additional effect of lowering the mosaicity as cryoprotection generates stresses due to changing solvent conditions and temperature induced volume changes. Our chip can be inexpensively mass produced and is simple to operate without the need of controlling valves.

The long term vision is to create a chip that uses temperature and concentration gradients to discover optimal crystal growth conditions [84]. Next, crystals would be grown at the optimal conditions to create a stream of tiny crystals that would be serially conveyed to a

part of the chip with ultra thin windows for in-situ diffraction. For this we are exploring windows made from materials such as ultrathin silicon nitride [102] or graphene [104], and ways to reduce in-beam volumes of the fluids surrounding crystals.

2.8 Acknowledgements

We thank Kelsey Anthony for helping with the D1D2 and glucose isomerase purification and D1D2 crystallization trials, Frank Mello from the Brandeis Machine Shop for fabricating the stainless steel magnet adapter, and Daniel Pommeranz Krummel, Irina Kriksunov, David Schuller, Chae Un Kim, Mike Cook, and Scott Smith for discussions and help with the protein X-ray crystallography. This work was supported by the NSF Brandeis MRSEC (DMR-0820492) and NSF MWN 1209518. CHESS is supported by the NSF & NIH/NIGMS via NSF award DMR-0936384, and the MacCHESS resource is supported by NIH/NIGMS award GM103485.

Chapter 3

Protein Crystallization via Controlled Evaporation from X-ray transparent Microfluidics

This chapter is on a collaborated project with *Michael Heymann* at CFEL, Hamburg.

Abstract

X-ray semi-transparent microfluidics is a technology that optimizes the kinetics of crystallization, eliminates crystal handling, eliminates cryo-protection and simplifies the collection of diffraction data for protein crystallization. The microfluidic device, which consists of thin patterned PDMS layer of 80 microns thickness containing hundreds of protein crystals in wells. The sealing or the "lidding" of the X-ray semi-transparent microfluidic devices are done using thin polymer materials, in order attain a high signal to noise ratio at the synchrotron, by reducing the background signal. Therefore the device carries an inherent

property of water permeation from the crystallization mix through this thin lid to outside. Here we exploit this property to manipulate the kinetics of protein crystallization. We increase the supersaturation of protein inside the stored drops by controlling the evaporation. Protein drops inside the chips shrinks via permeation. As water evaporates from the drop, the solute concentrations inside the drop increase, so does the protein supersaturation. We investigate how the crystallization kinetics and hence the number of crystals and morphology of the crystals change with different evaporation rates.

3.1 Introduction

Protein crystallization remains the bottleneck in determining the structure of proteins. When determining the structure of a protein, the crystal should preferably be largest as possible and grown under defect free condition in order to facilitate requirement of obtaining all the necessary X-ray diffraction data from a single crystal and merging data sets, respectively. Given that such a crystal exists for a particular protein, we attempt to optimize the process conditions by finding optimal equilibrium and kinetic pathways to get that crystal. Despite the fact that thus far experiments have failed to reveal the details of nucleation, crystallographers attempt many different methods such as bulk dialysis, batch method, vapor diffusion, microdialysis, etc. Among all these methods vapor diffusion is the technology from which the majority of protein have been crystalized [62]. In vapor diffusion, a drop composed of a mixture of protein and precpitant is placed in vapor equilibration with a liquid reservoir of precipitant. The drop contains a lower precipitant concentration than the reservoir. Water vapor leaves the drop goes to the reservoir. As water leaves the drop, the supersaturation of the protein mixture monotonically increases. Eventually a crystal will nucleate but you may not be in the equilibrium state yet and hence there could be an overshoot and may be you

get many crystals. Also, when the first crystal is nucleated the supersaturation at high such that there is a high inter-particle potential, so the energy could be too high for the defects to anneal and hence this might not be the optimal growth condition.

In this study, we attempt to mimic vapor diffusion trials using X-ray semi transparent microfluids with controlled evaporation rates. We fabricate X-ray semi-transparent version of the revised PhaseChip [84, 83] storage layer described in section 4.3 of [38]. We use "store-then-create" [9] method to form surfactant stabilized aqueous drops in the storage layer which contains hundreds of 34 nL wells where protein solution is stored. The difference in chemical potential of water inside a drop and outside drives the flow of water across the thin lidding material. The direction of this gradient is such that water flows out of the drops, therefore shrinking them and increasing the solute concentration. Several independent control layers are used on the chip for both spatial and temporal control over the protein concentration in the drops.

3.2 Controlled Evaporation

X-ray semi-transparent version of the PhaseChip consists of an array of cylindrical wells of 600 μm diameter and 120 μm tall using PDMS and two 8 μm thick Kapton foils on top and bottom for sealing. The fabrication method is described in section 2.3. The bare device (without the chip-to world interfacing) is 80 μm thick as shown in Figure 3.1(a). We adapt the model described in [83] to describe our system. Due to the chemical potential gradient of water (∇C_{water}) inside and outside the drop there exists an outward flux of water $J = -P\nabla C_{water}$, where P is the permeation coefficient of the material outside the drop. In order to have better control over the evaporation for this study, we constrain the evaporation such that the water permeates through one lid of the device by plasma-bonding

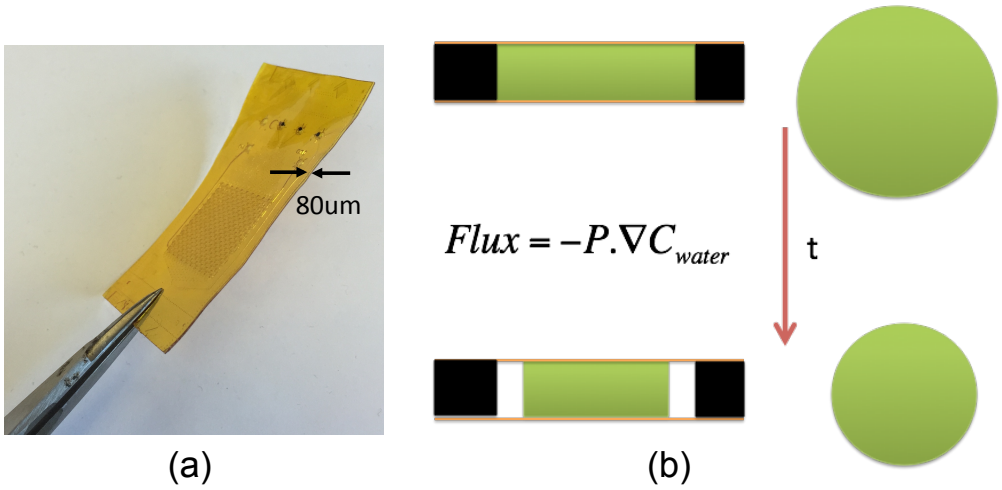

Figure 3.1: (a)The effective thickness of the X-ray semi-transparent device is 80 μm with PDMS featured wells of 50 μm in height where the protein and the precipitant mixture is stored. The sealing is done with 2 Kapton foils of 8 μm thick. (b) The cross sectional view (left) and the top view (right) of a well containing a protein drop. the outward flux from the drop to the outside is $J = -P\nabla C_{water}$. The

a microscope slide instead of one Kapton seal . In our model, we assume negligibly small lateral evaporation. Once the water evaporated out of the drop, the drop shrinks with time as schematically shown in Figure 3.1(b).

In all the experiements conducted for this study, we use **Glucose isomerase** as the protein of interest. The storage layer of the PhaseChip was first primed with 12 wt% Fluorooctanol in FC-43 oil. The drops were created *on-chip* with the mixture of 15 mg/ml glucose isomerase from *Streptomyces rubiginosus* (from Hampton Research), 50 mM ammonium sulfate, pH 7.0, 10 wt% PEG 10,000 in a 1 : 1 ratio (all from Sigma Aldrich).

In order to attain a wide range of evaporation rates, we employed several methods to integrate a control layer on top of the Kapton foil which is open to air though which the water evaporate out of the drop. To attain slowest evaporation rates we mounted a reservoir of 1M, 2M or 3M $NaCl$ solution on the Kapton foil. A custom acrylic window and shield was cut to shape from 3 mm thick acrylic sheet using 40 W CO_2 Hobby Laser cutter (Full Spectrum

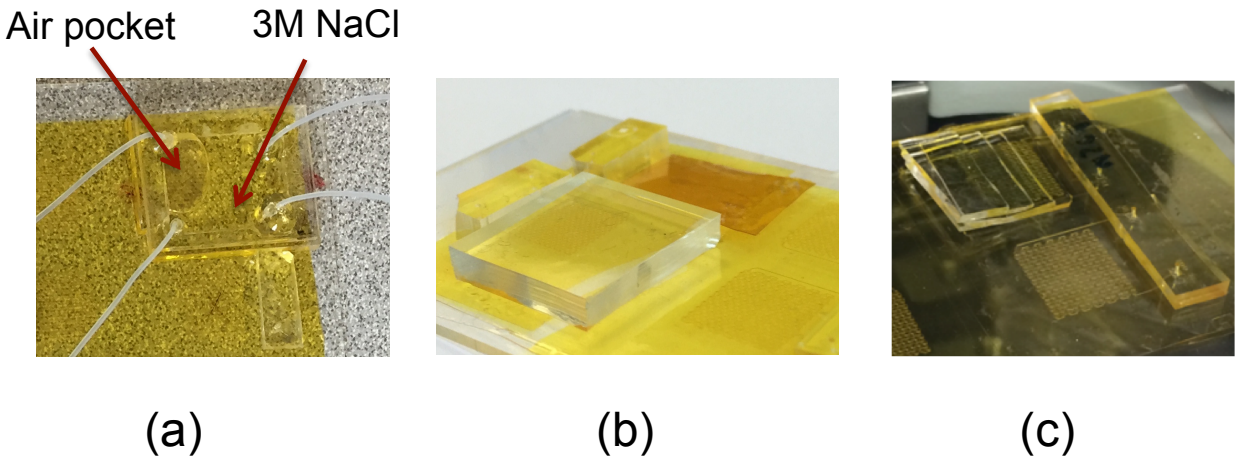

Figure 3.2: (a) $NaCl$ reservoir on the device.(b) PDMS slab and Adhesive Kapton tapes on the device. (c) Staggered PDMS sheets on the device to attain heterogeneous evaporation rates.

Laser) and assembled with 5-min epoxy glue to fabricate the reservoir. Figure 3.2(a) shows the plumbing necessary to fill the chamber with the $NaCl$ solution and a partially filled reservoir for visual aid. We also use thick slabs of PDMS of adhesives Kapton tapes on the Kapton foil as control layers to attain a variety of evaporation rates as shown in Figure 3.2(b). With these methods we could attain an order of magnitude large evaporation rate range. In the cases where we needed to observe heterogeneous supersaturation profiles over the device we used a stack of PDMS sheets staggers to obtain different polymer thicknesses in the different regions of the device to attain a rage of evaporation rates in the same device.

3.3 Evaporation rate

We scanned the regions of device at a regular intervals of 30 mins using a homemade robotic stage that can scan and acquire images [5]. The stage is equipped with two thermoelectric coolers (TECs) to control the temperature and hence we maintained the temperature at

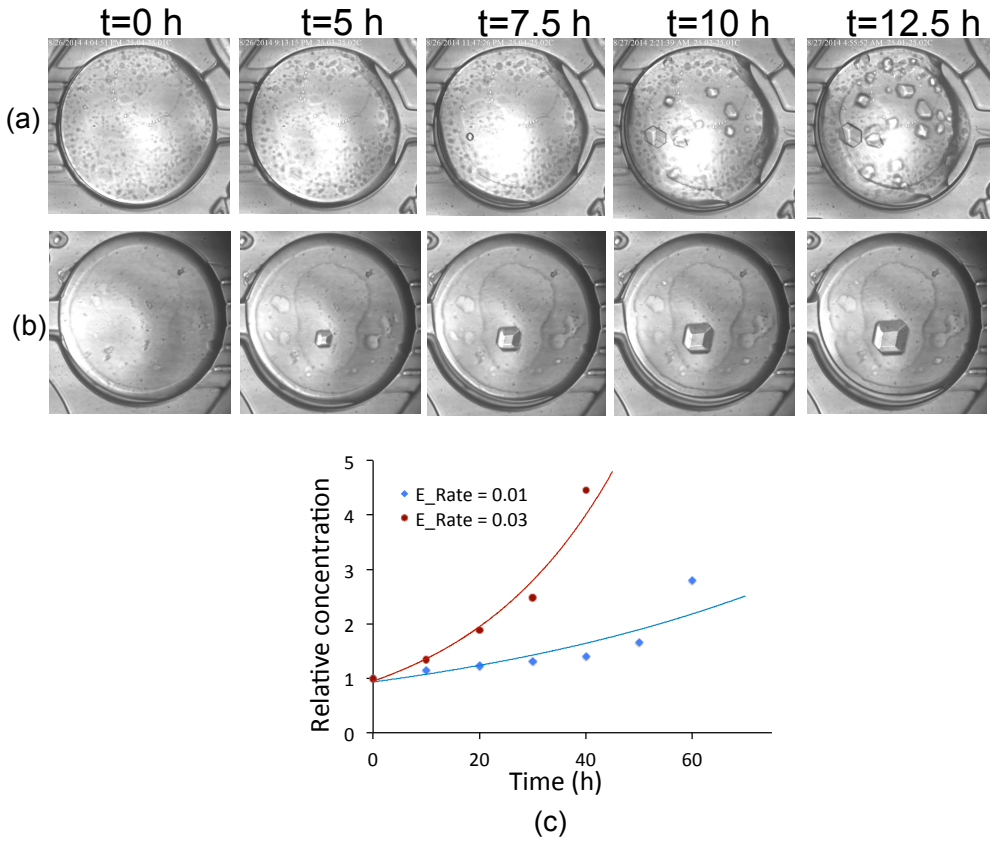

Figure 3.3: Time-lapsed images one a drop of (a) 30 crystal and (b) one crystal along with their (c) concentration profiles.

25°C. The relative humidity was maintained at 40%. Figure 3.3(a) and (b) rows show the time lapsed images of two chosen drops. The solution interface or contact line of each drop was used to obtained the area of the remaining solution along with the "freehand selection" tool in ImageJ 1.47 [71]. The area and hence the volume occupied by the solution in each well was determined as a function of time, since we assume the height of each drop remains constant. The concentration of the precipitant and protein solution is inversely proportional to the volume. The evaporation rates were represented by the reciprocal time constant of each concentration profile as shown in the Figure 3.3 (c) for the two drops considered here.

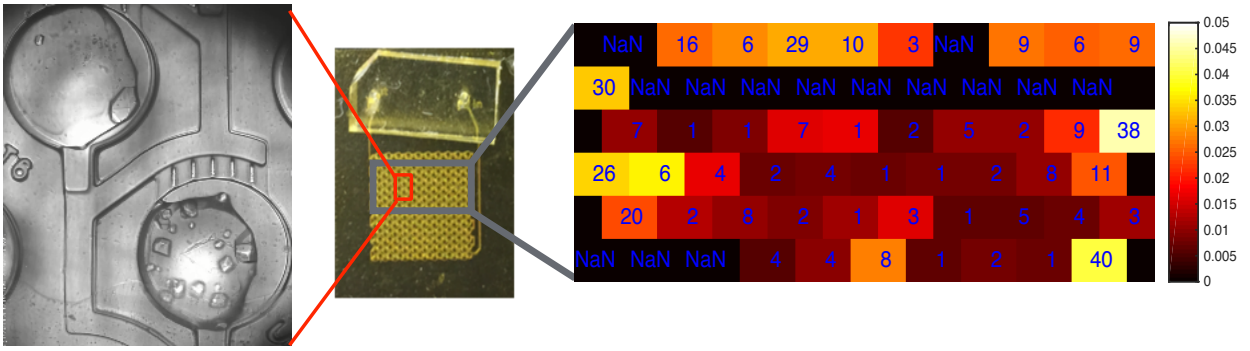

Figure 3.4: Right: The color map indicates the evaporation rate of each drop, corresponding to it's spatial orientation in the device and the numbr of crystals in each drop from the digit placed on a well. "NaN" stands for the drops which were not being analyzed due to poor loading of the solution. This evaporation profile of the device has been obtain by the staggered PDMS stack showed in Figure 3.2(c). Middle: The top view of the device and the spatial orientation of the color map. Left: Two drops from a randomly selected area has been zoomed in to show the number of crystals per drop vary with the evaporation rate.

3.4 Number of Crystals per Drop

The heterogeneous evaporation profile over a portion of a device is shown in the color map of Figure 3.4. The protein drops inside the chips shrink as water evaporates from the drop, the precipitant concentrations inside the drop increases, so does the protein supersaturation. Different evaporation rates give rise to different supersaturation profiles and hence to different nucleation rates. The drops with different evaporation rates bare different number of crystals and the color map indicates the number of crystals each drop contains.

The histograms in Figure 3.5(a) show how the number distribution of the crystals per drop change as the evaporation rate changes. Supersaturation inside the drop is lower for lower evaporation rates and the there are fewer crystals nucleate in the drop. A qualitative analysis could conclude that the nucleation via controlled evaporation is a non-Poisson process. Our results are in the poor agreement with Galkin and Vekilov's finding where they observe nucleation being Poisson process via temperature quench [27]. But we do see the nucleation

process approaches to a Poisson process at very low evaporation rates where the number of crystals per drop closely relates exponentially with time in Figure 3.5(b).

3.5 Imaging in SHG, UV and and X-ray

Second Harmonic Generation (SHG) microscopy is based on the emission of coherent light at exactly twice the frequency of the incident light. Non-centrosymmetric molecular polarizability can lead to SHG and thus any chiral protein crystal can give a SHG signal [65], while disordered or centrosymmetric packings of the same individual proteins cannot. From previous studies we knew that our device doesn't interfere with the SHG signal [38]. Crystals were observed inside the chip using bright field microscopy Figure 3.6(a) (top), and SHG imaging Figure 3.6(a) (bottom) using the SONICC imaging platform (at Formulatrix, Bedford, MA) with 10x objective. Glucose isomerase crystals gave strong SHG signal and the SHG imaging helped identifying the crystalline structures which weren't apparent under the scanned images.

Most proteins contain tryptophan, which when excited by UV light will fluoresce at between 300-350 nm. Given that protein crystals are concentrated areas of protein, they should glow brightly when illuminated with UV light. The UV imaging allows one to locate protein crystals and to validate that the crystal is a protein crystal and not a misleading salt crystal. Two criteria that have to be met for UV fluorescence to be observed: the protein must contain chemical groups capable of absorbing energy at the excitation wavelength and the emitted energy has to avoid intermolecular and intramolecular absorbance (fluorescence quenching) [16]. The non-crystalline aggregates of protein could also fluoresce when excited by UV light. Therefore, a combination of SHG and UV microscopy will make one certain about where there is a crystalline structure and that structure is comprised of protein.

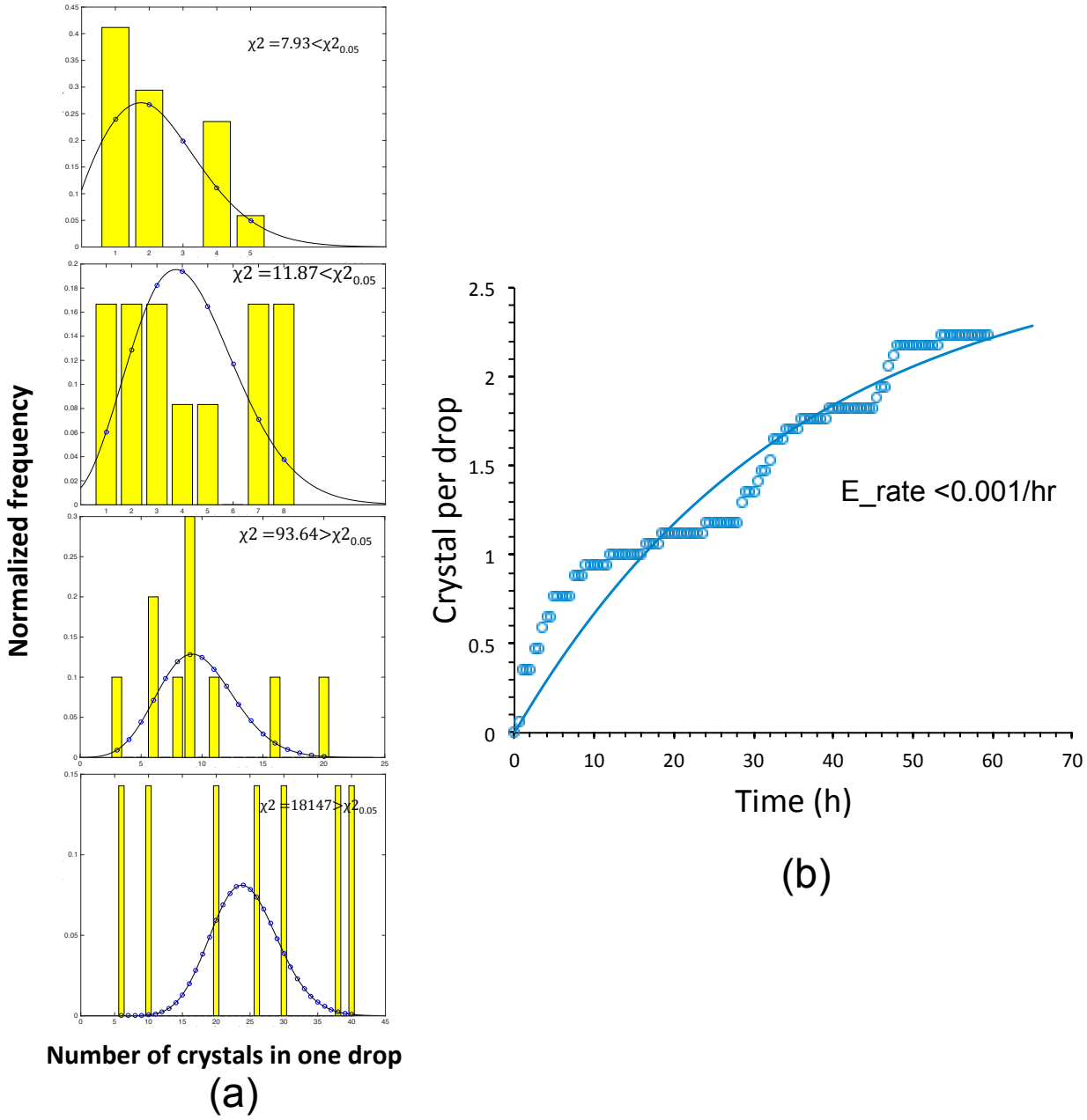

Figure 3.5: (a) Distributions of Glucose Isomerase crystals per drop at different evaporation rates plotted along with their Poisson distributions. The Chi values are given for each distribution. (b) Nucleation approaches to a Poisson process at very low evaporation rates where the number of crystals per drop closely relates exponentially with time

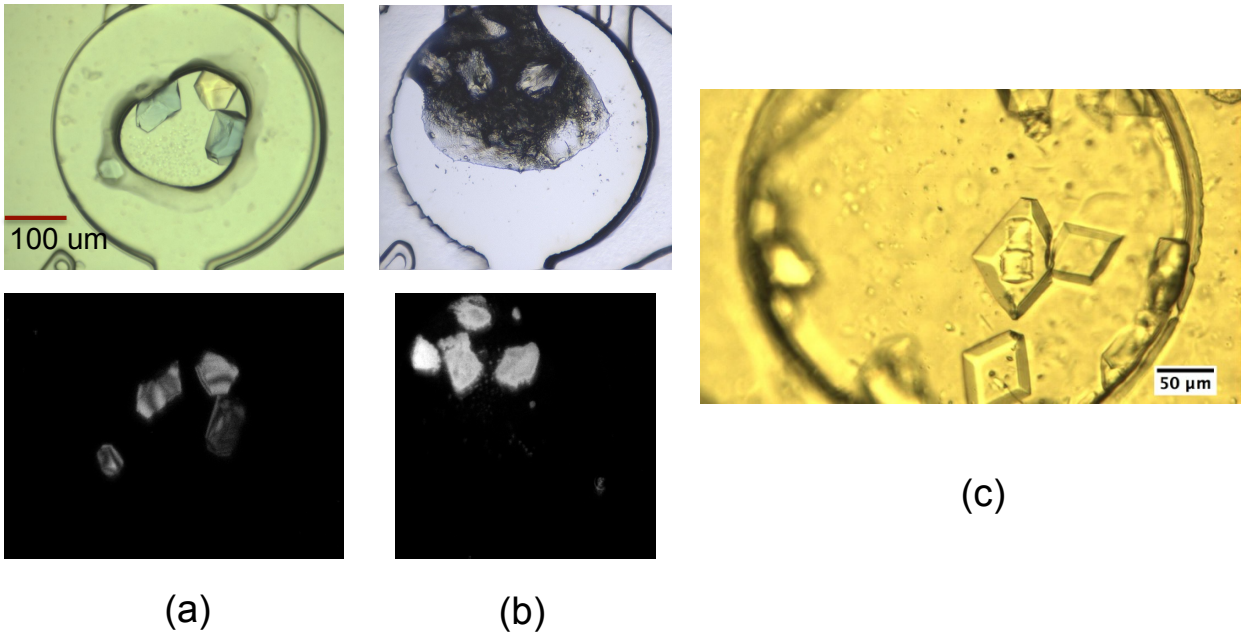

Figure 3.6: (a)Glucose isomerase crystals in the X-ray semi-ransparent PhaseChip imaged with (a) top: bright field microscopy and (a) bottom: with SHG. (b) bottom with UV fluorescent. (c) The first crystal that was shot with X-ray beam twice to find appropriate exposure times.

We observed protein crystals under UV imaging under same SONICC platform mentioned above. We had to peel off the Kapton foil lids to see excite our crystals with UV since the Kapton absorption overlaps in the UV region of the spectra. After we removed the Kapton foil, the crystal drop dried off in 2-3 minutes, and hence the bright field image shown in Figure 3.6(b) (top) did not help much identifying protein crystals. But the UV image Figure 3.6(a) (bottom) revealed that there was protein and along with the SGH image we could conclude that they are crystals.

The full devices (with Kapton lid both sides) were used to grow crystals with controlled evaporation and X-ray diffraction data were collected at Petra III, P11 and P14 beam lines *(see appendix 2)*. 100 frames with 0.1 degree oscillation each from 85 crystals in total were collected from around 30x30 μm Glucose Isomerase crystals with a roughly 20x20 μm beam.

Actual recordings happened at about 30 ms exposure time.

3.6 Conclusion and Future work

We developed simple and robust X-ray semi transparent microfluidic device to carry out experiments to investigate the effect of controlled evaporation on protein nucleation and crystallization and X-ray diffraction studies. We have mange to attain homogenous and heterogeneous evaporation rate profiles over the X-ray semi transparent microfluidic devices reproducibly, using simple methods such as stacking polymers as the control layer. Many groups have studied the effect of evaporation on nucleation as a pathway to protein crystallization, with and without [59, 60, 75] the use of microfluidic device. Nevertheless, the studies on microfluidics devices incorporated pneumatic valves in the chip [34, 33], making them laborious to manufacture and hard to operate.

Moving to the rapid prototyping of thermoplastics such as Cyclic olefin copolymer (COC) which has better optical properties, will be a better alternative to encourage the structural biology community to use the X-ray semi-transparent microfluidic devices for crystallization and diffraction studies. We tested the quality of the crystals grown in these devices via controlled evaporation using three major imaging techniques; SHG, UV and XRD and conclude that we grew diffraction quality crystals of Glucose Isomerase using this technique.

The on going analysis will present a qualitative information about the nucleation process via controlled evaporation being non-Poisson. Another interesting aspect to investigate is the volume dependance on the evaporation rate studies. Preliminary results have shown (data not shown here) us that the protein drop of 4nL size, show non-Poinsson behavior even at the lower evaporation rates. Exploring this quantitatively is the continuation of this study since both evaporation rate and volume are non-thermodynamical parameters and

hence will give us an insight of the kinetics of protein nucleation.

3.7 Acknowledgement

We thank Ellen Gualtieri at Formulatrix for helping us to use their SONIIC instrument to capture SHG images and Cornelius Gati for helping with python script running to have the X-ray diffraction data indexed and merged (Petra III P14 line)

Chapter 4

Low-Z polymer sample supports for fixed-target serial femtosecond X-ray crystallography

This chapter is adapted from [25] which is published at the journal *J. Appl. Cryst.*

Abstract

X-ray free-electron lasers (XFELs) offer a new avenue to the structural probing of complex materials, including biomolecules. Delivery of precious sample to the XFEL beam is a key consideration, as the sample of interest must be serially replaced after each destructive pulse. The fixed-target approach to sample delivery involves depositing samples on a thin-film support and subsequent serial introduction via a translating stage. Some classes of biological materials, including two-dimensional protein crystals, must be introduced on fixed-target supports, as they require a flat surface to prevent sample wrinkling. A series of wafer

and transmission electron microscopy (TEM)-style grid supports constructed of low-Z plastic have been custom-designed and produced. Aluminium TEM grid holders were engineered, capable of delivering up to 20 different conventional or plastic TEM grids using fixed-target stages available at the Linac Coherent Light Source (LCLS). As proof-of-principle, X-ray diffraction has been demonstrated from two-dimensional crystals of bacterio- rhodopsin and three-dimensional crystals of anthrax toxin protective antigen mounted on these supports at the LCLS. The benefits and limitations of these low-Z fixed-target supports are discussed; it is the authors' belief that they represent a viable and efficient alternative to previously reported fixed-target supports for conducting diffraction studies with XFELs.

4.1 Introduction

The recent availability of X-ray free-electron laser (XFEL) light sources has extended the ability of X-rays to probe biomolecular structure [13, 80, 24, 85]. The high X-ray flux (1012 photons) and ultrashort (30 fs) durations of XFEL pulses enable data collection from smaller crystals and of shorter temporal resolution than other crystallographic methods. Beginning with three-dimensional nanocrystals of Photosystem I [13] increases in X-ray energy coupled with advances in experimental apparatus have incrementally added high resolution [10], previously unknown structures [72], de novo phasing [7] and light-induced pump probe capabilities [6, 49, 51, 90] to the structural biology XFEL toolbox.

Because XFEL bio-imaging experiments rely on the 'diffraction-before-destruction' principle [65], a single specimen, such as a single molecule, three-dimensional or two-dimensional crystal, can only give rise to one diffraction pattern. Consequently, fresh sample must be serially delivered to the XFEL pulse. Lomb et al. [54] coined the term 'serial femtosecond crystallography' (SFX), referring to an experiment performed with crystals of biological

macro- molecules [13, 54]. The gas dynamic virtual nozzle (GDVN), the first delivery mechanism for SFX, successfully injects fully hydrated crystals into the XFEL beam [100]; however, the fast linear velocity ($\geq 10ms^{-1}$) required to maintain a stable jet results in only an exceedingly small fraction (less than 0.1%) of the sample being probed by X-rays at 120 Hz, as this is the fastest repetition rate of the Linac Coherent Light Source (LCLS). This in turn leads to significant sample consumption requirements to complete an SFX experiment. One solution to this sample consumption dilemma is manifested in a lipidic cubic phase (LCP) injector, whereby crystals suspended in viscous LCP extrude from the injector at a significantly reduced velocity [101]. However, the applicable sample space with this injector is limited to LCP-compatible biological systems, namely integral membrane proteins. Furthermore, neither GDVN nor LCP injection technologies are appropriate for two-dimensional crystallography (2DX), which requires crystals to be kept relatively flat, generally on a support. 2DX represents an attractive method for structure determination of biomolecules, especially membrane proteins, given the reduced amount of sample required to form two-dimensional crystals and the near-native environment provided by a planar lipid bilayer. Another strategy, fixed-target serial femtosecond crystallography (FT-SFX), accomplishes both a reduction in sample consumption [41] and sample presentation on a flat surface at a fixed and known angle. For a typical FT-SFX experiment, samples are deposited on a wafer containing X-ray transmissible windows consisting of a thin film or membrane, e.g. 20 - 50 nm-thick Si3N4, and serially introduced into the beam via a translating stage [26, 41, 68].

Radiation damage associated with the long exposure times required at conventional X-ray sources (synchrotron and home source) prohibits structure determination by X-ray diffraction in transmission from two-dimensional lattices. On the other hand, the shallow penetration of electrons in biological materials limits their utility for three-dimensional crystallography (3DX). Thus, in general, transmission electron microscopy (TEM) enables 2DX while X-

rays are used in 3DX. Using an FT-SFX approach, X-ray diffraction in transmission from two-dimensional crystals was recently demonstrated for the first time [26] to 7 Angstrom resolution [68], using the membrane protein bacteriorhodopsin (bR). Furthermore, the recent demonstration of electron diffraction from sub-micrometer three-dimensional crystals of lysozyme (microED) and subsequent structure solution has extended the capabilities of TEM [64, 82]. Therefore, the sample accessibility space for X-ray and electron diffraction is converging. In order to complement FT-SFX studies of two-dimensional and three-dimensional crystals, we have developed the tools and methodology to bridge XFEL and TEM techniques for sample preparation and delivery at XFELs. Here we report on the design, production and performance of low-Z polymer constructed TEM-style mesh grids and wafers tailored to XFEL experiments. We constructed a fixed-target sample support holder capable of delivering up to 20 polymer TEM grids, as well as conventional (metal mesh) grids, for data collection, taking advantage of the ability of FT-SFX to deliver samples at a known angle and reduced sample consumption. Proof-of-principle X-ray diffraction experiments were conducted using both 0.1 and 1 mm beam focus sample environments of the Coherent X-ray Imaging (CXI) instrument [10, 53] at the LCLS.

4.2 Design and construction

Two important considerations for FT-SFX include minimizing sample consumption (volume per shot) and maximizing the data acquisition (DAQ) rate (shots per time). Because these experiments are conducted under vacuum in a chamber of limited size, overall DAQ rates are further constrained by the time required to vent and pump down for each sample change. Thus, for a given sample set, DAQ efficiency is also dependent on window density (shots per area). For a typical FT-SFX experiment, samples are deposited on individual support wafers

with footprints of 25 x 25 mm or 25 x 12.5 mm. These wafers are then mounted on a fixed-target apparatus consisting of $7500mm^2$of X-ray accessible space (as of July 2014). Stepper motors control the x, y and z translation, as well as the tilt angle around the x axis. DAQ rates of 10 per second have been shown for three-dimensional crystals on longer windows [41]; however, under the allowed experimental conditions and considerations observed in this report DAQ is generally limited to shot-on-demand mode for two dimensional crystals on fixed targets, 1-2 second, as each individual window must be translated and aligned with the beam. In developing a suite of sample support devices for FT-SFX, we strove to reconcile traditional TEM sample preparation methods with the FT-SFX experimental constraints mentioned above. We surmised that sample consumption and window density could be simultaneously addressed using a canonical TEM grid, which requires only a minute sample volume ($2\mu l$) and small linear footprint (3.05 mm diameter). Most commercially available TEM grids are fabricated from a conductive metal to alleviate specimen charging during electron exposure [19] and are varied in terms of material composition and mesh size. For our design model, we considered tabbed (alias, 'handle') grids to exploit the additional tab bulk in orienting the grid for optimized data acquisition. We chose the Veco handle 150 copper square mesh grid with window dimensions 127 mm on an edge and a bar width of 40 mm. The relatively large hole provides some leeway for alignment, beam wings or other experimental factors that would lead to intense X-ray scattering from the copper mesh. Grids were custom ordered pre-deposited with 5 nm thick carbon support film (Electron Microscopy Sciences, Hatfield, PA, USA).

4.3 Design and fabrication of plastic grid and wafer components

Since diffraction by X-rays is not limited by sample charging during exposure as it is for TEM, the construction of support grids from a conducting metal is superfluous. Indeed, replacing the metal with a lower-Z polymer alleviates many of the concerns of the intense X-ray beam scattering from the metal support. We used SU8-photoresist (MicroChem Inc., Westborough, MA, USA) as the substrate for a polymer constructed sample support. SU8-photoresist provides for the possibility of inexpensively mass producing an optimized design for potential high-throughput SFX applications. To ensure mechanical stability and maintain two-dimensional crystal sample flatness, we used a two layer design of 225 μm total thickness (Figure 4.1(a)). We designed and fabricated our initial polymer grid (referred to herein as 'plastic grid') with the same footprint as the Veco handle grid described above (Figure 4.1(b)). These grids have windows of dimensions 127 x 127 μm with separating bars of thickness 40 mm, giving rise to 120 μm 120 full windows that are X-ray accessible (using either the 0.1 or 1 μm foci of the CXI).

Inspired by the rectangular design and subsequent high window density of the conventional Si3N4 sample support wafers employed in the initial FT-SFX experiments at the CXI ([26, 41, 68]) we also fabricated a wafer from SU8-photoresist (referred to herein as 'plastic wafer') in a similar manner to the plastic grids (Figure 4.1(c)). These wafers have a 25 x 12.4 mm footprint, and their thicker SU8 support component consists of 17 x 8 units containing smaller XFEL-accessible windows, creating a 'window-in-a-window' design. While the added support restricts the available window space, this design still permits thousands of shots per wafer, depending on the window dimensions chosen. For example, the 100 x 100 μm window design we fabricated with 50 μm spacing provides 4896 X-ray accessible

windows. By contrast, a comparable Si3N4 wafer of 44 rows and 18 columns contains only 792 windows. Furthermore, compared to Si3N4 wafer fabrication, plastic grids are easier and faster to produce and hence allow for a more straightforward custom-design and fabrication platform of the window shape and dimension. The wafer in Figure 4.1(d) contains windows of 100 x 400 μm, and windows of 100 x 100 μm were also fabricated and tested. One could conceive a 100 x 400 μm design for a 2DX tilt series, or a significantly longer window for fast FT-SFX data collection at 10 Hz [41].

Plastic grids and wafers were designed using the *AutoCAD* software suite (Autodesk, San Rafael, CA, USA) and translated into photo-masks through a commercial service (CAD/ART Services Inc., Bandon, OR, USA). They were then fabricated from SU8-photoresist on silicon wafers that were pre-treated to facilitate detaching of finished supports during SU8 development. A 28 nm thick Omnicoat (MicroChem) release layer was prepared on the 3 inch (1 inch = 2.54 cm) polished wafer (P(100) 0 - 100Ωcm SSP 380 μm Test Grade from University Wafer) by spin-coating at 500 r min^1 for 5 s, followed by 3000 r min^1 for 30 s, and then hard-baked at 473 K for 1 min. We then deposited a 25 mm layer SU8-3025 (MicroChem) for the window mesh followed by two additional SU8-2075 (MicroChem) layers of 100 mm thickness each for the support frame that reinforced the window mesh Figure 4.1(a). This sequential build-up, rather than preparing a 200 μm film in a single step, was necessary to achieve the required accuracy for wafer thickness. Furthermore, the edge bead incurred from the sequential build-up was consistently smaller, allowing for more accurate alignment. Generally, SU8 layers were prepared by spin-coating and baking according to the manufacturer's specifications; however, some deviations were required to maintain accuracy for thickness and substrate flatness. These included spin-coating the second 100 μm layer onto the first 100 μm layer immediately after it had been softbaked and doubling the UV exposure dose from 240 mJ cm^{-2} recommended for 100 μm to 2 x 240 mJ cm^{-2} for the

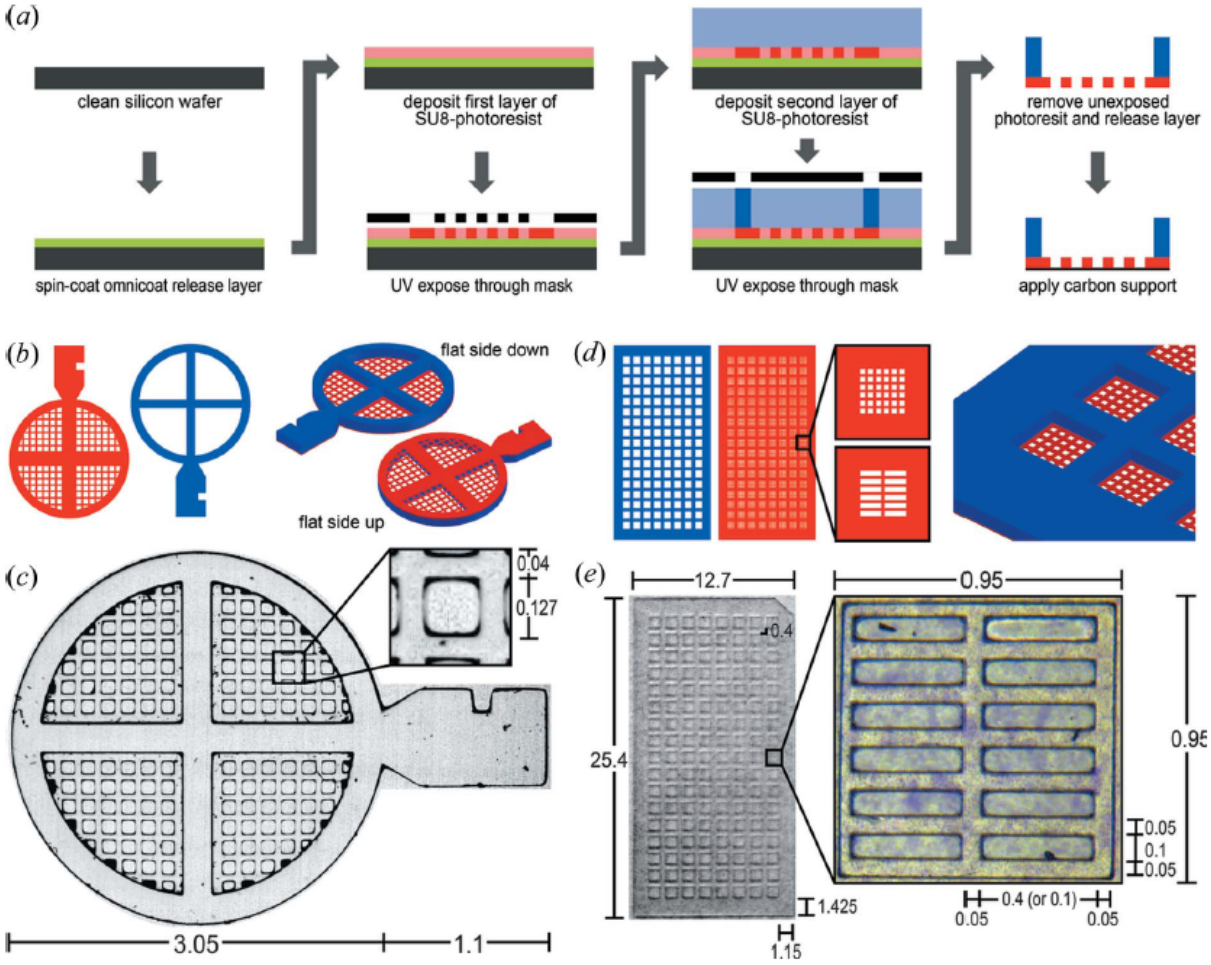

Figure 4.1: (a) Schematic of the fabrication process. After an Omnicoat release layer (green) a 25 mm layer of photoresist (red) is deposited and selectively cross-linked using UV light and a photomask. Subsequently a second 200 mm thick layer of photoresist (blue) is deposited and patterned. Finally all uncured (unexposed) photoresist as well as the release layer are developed away and detached grids receive a carbon support to hold sample. (b) Plastic grid components rendered as CAD drawings. (c) Micrograph of an assembled plastic grid. The overall and window/bar dimensions are identical to the 150 mesh handle grid on which this particular design was based. (d) Wafer grid components rendered as CAD drawings. Both grids (b) and wafers (d) are constructed from two separate pieces, one containing the windows (red) and the other providing structural support (blue). Three-dimensional renderings of assembled grids (a), (right) and wafers (d), (right). (e) Micrograph of an assembled plastic wafer. The zoom-in micrograph shows the wafer used in this study with bR purple membrane adhered to carbon support with window dimensions 100 x 400 μm. Windows of dimensions 100 x 100 μm were also fabricated. All measurements are in mm.

2 x 100 μm support frame. SU8 flows during the pre-exposure bake, resulting in a slight wedge-shaped cross section if it is not on a perfectly leveled surface. This effect is more pronounced at the longer baking times required for thicker layers. To further improve alignment accuracy of window mesh and support frame, we used a vernier caliper based alignment mark and a selective alignment mark development scheme [37]. After the final post-exposure bake, uncured SU8 and the Omnicoat release layer were developed away by washing in a bath of propylene glycol monomethyl ether acetate (Sigma?Aldrich, St Louis, MO, USA) overnight. The grids and wafers were then rinsed and stored in 2-propanol (Sigma?Aldrich) for transport. The choice of support film to apply to plastic grids or wafers is experiment dependent. For initial experiments carried out at the LCLS, 8 - 20 nm thick carbon films were floated onto the grids, either in bulk by lowering the film onto water submerged grids, or individually by picking up 16 mm^2 carbon film pieces on 0.5 - 1 ml droplets of Milli-Q purified water (EMD Millipore, Billerica, MA, USA) and standard practices [1]. Carbon films of varying thickness, up to 20 nm, were applied to submerged plastic wafers by carefully lowering the film floating on a Milli-Q water surface. For three-dimensional microcrystal trials, we applied thin films of 1%(w/v) polyvinyl formal (in 1,2-dichloromethane) to plastic wafers at the air-water interface using standard methods.

4.4 Sample preparation and application

For our initial proof-of-principle FT-SFX studies of low-Z polymer supports, we used two-dimensional crystals of bR deposited on plastic grids and wafers. Preparation of purified bR patches followed methods reported previously [26]. Aliquots (2 - 3 μl) of 1 - 3 mg/ml of bR were applied to the film side of UV cleaned plastic grids sporting carbon support film by holding the grid in air with reverse forceps, allowing to air dry for 5 min and blotting

away excess solution. As proof-of-principle for FT-SFX studies of three-dimensional crystals of anthrax toxin protective antigen on plastic wafer supports, we used a microcrystal - oil immersion technique as described previously [41]. The crystal-oil immersion was adhered to plastic wafers sporting 1%(w/v) polyvinyl formal as the support layer by spreading with the edge of a 10 ml Rainin LTS pipette tip (Mettler, Toledo, Columbus, OH, USA).

4.5 Conclusion

Here, we described viable plastic grids that may be specifically tailored for XFEL experiments without metal background scattering. We propose an experimental pipeline where samples are initially characterized by TEM using metal grids, which may be examined with XFELs for diffraction quality; further optimization under XFEL conditions is then screened with plastic grids designed specifically for the experiment under investigation. Furthermore, plastic grid designs that prove most useful for screening purposes can be easily and cheaply mass-produced for high throughput operation. We foresee that the substrate support components and methods described here will provide a useful mechanism for extending the capabilities of FT-SFX at XFELs.

4.6 Acknowledgemet

The authors acknowledge Dongshin Kim for help and discussions on grid fabrication, and Mukthi Kukkadapu and Emme Patello for sorting diffraction data.

Chapter 5

X-ray Transparent Microfluidics for Biomineralization

This chapter is on a collaborated project with *Michael Whittaker* and *Prof. Derk Joester* at Northwestern University

Abstract

Biomaterials composed of calcium carbonate range from ancient limestone deposits to modern marine reefs. Many organisms use Amorphous Calcium Carbonate (ACC) during the process of biomineralization as a way of controlling materials shape, size and phase stability. Despite this importance, a clear understanding of the fundamental processes controlling the crystallization of calcium carbonate is still lacking. Biomineralizing organisms frequently precipitate minerals in small phospholipid bilayer-delineated compartments. In previous studies, the growth and stabilization of liposome-encapsulated ACC has been investigated. We present a high throughput and robust method of studying ACC formation in confined

volumes using a X-ray semi-transparent microfluidic platform. This allows growing ACC using well-controlled conditions such as precise volumes, pH and osmotic pressure along with dynamical variations of supersaturation, combined with in-situ x-ray diffraction data collection. We will describe the microfluidic device, which consists of thin patterned PDMS layers containing hundreds of storage regions for individual reactions of forming ACC along with a carbon dioxide reservoir underneath, sandwiched between two thin Kapton sheets.

5.1 Introduction

The aims of this project are to stabilize ACC in confined volumes using microfluidics devices and probe the formation mechanism of ACC using small angle X-ray scattering technique. Metastable amorphous minerals are used in growing biological crystals [2] such as amorphous calcium phosphate in bone mineralization [57], as a precurser. Confining ACC in cylindrical pores of track-etch membranes [77], on arrays of picoliter droplets created on patterned self-assembled mono-layers [88] and in liposomes [92, 91] has been reported in earlier studies. However these processes are either cumbersome or suffer from lack of control over the physical or chemical parameters such as size of the confinement, pH, concentration of the solutes, etc. These parameters are vital to the on going studies such as nucleation rate of crystalline polymorphs of calcium carbonate, growth, mechanism and kinetics of transformation of ACC to crystalline polymorphs in solution, role of water in the process phase transformations and influence of additives . The question of whether ACC form by nucleation or spinodal decomposition is still open for discussion. Very little experimental work is being done with competing conclusions [23, 31] and hence finding good experimental evidence for whether ACC forms by spinodal decomposition or nucleation, by catching the early events of ACC formation is a high value target.

Liposomes exhibit heterogeneity in size. Also, there is very less control over the size of the liposomes one needs for experiments demand high statistics. To precisely control the size and the stability of the confinement, we use microfluidically produced and surfactant stabilized water-in-oil drops as liposome analogues with a controlled supply of additives. Previously we developed X-ray semi-transparent microfluidic devices for protein structure determination [39]. With the "PhaseChip" [84] it is shown that manipulating the osmotic pressure of the solution is an effective way to control the solute supersaturation, for example in order to decouple crystal nucleation from crystal growth. We propose to fabricate X-ray semi-transparent version of the PhaseChip to effectively stabilize the metastable ACC and to carry out scattering experiments with small angle X-ray scattering (SAXS) technique. Time-resolved SAXS study has been previously done to investigate of the effect of a double hydrophilic block-copolymer on the formation of calcium carbonated [8], using a stopped-flow cell for rapid mixing of the reactant solutions. Same author has developed a robust microfluidic system for solid particle imaging using SAXS [86] but does not mention calcium carbonate as a potential application. We expected that SAXS characterization of supersaturated calcium carbonate solutions within the X-ray semi-transparent microfluidics device, before the precipitation of ACC will reveal the signatures of a spinodal decomposition if such a mechanism is at work. Although we haven't successfully taken SAXS data on the early stages of ACC formation with our microfluidic device yet due to the technical difficulties at the SAXS beam line, we have obtained wide angle X-ray (WAX) data on stable polymorphs of calcium carbonate with our microfluidic device as a proof of principle and also have obtained interesting results on stabilizing ACC in microfluidic confinement.

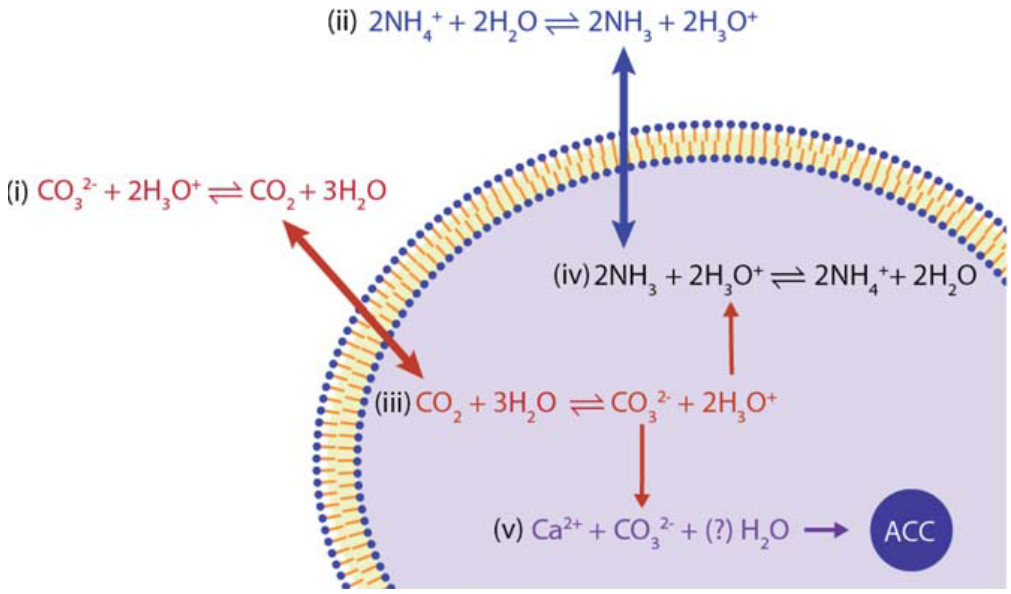

Figure 5.1: On the outside of the liposome, carbon dioxide (i) and ammonia (ii) are present in equilibrium with carbonate and ammonium ions in the ammonium carbonate solution. The neutral species diffuse across the membrane. (iii) Hydration of Ca^{2+} to $CO_3{}^{2-}$ releases protons that lower the pH inside the liposomes. Co-diffusion of ammonia (iv), driven by its conversion to $NH_4{}^+$ buffers the pH on the inside of liposome. Finally, the coupled equilibria are drained by precipitation of ACC (v) from encapsulated calcium and carbonate formed in (iii). The original figure and the description is from [92].

5.2 Liposome analogues in microfluidic device

We replace the previously used liposome system [92] with microfluidically made emulsion drops. Figure 5.1 explains the reaction domain of the calcium carbonate system inside a liposome. We use "store-then-create" [9] method to form surfactant stabilized aqueous drops in the revised version of PhaseChip storage layer described in section 4.3 of [38].

We fabricated the X-ray version of the PhaseChip for studying ACC formation. PhaseChip consist of two layers; storage and the reservoir separated by a membrane made out of PDMS, which is highly permeable for gases. The storage layer consist of the and the reservoir layers are place above and below the permeable membrane respectively. The storage layer which

is an array of cylindrical wells of 600 μm diameter, and the reservoir layer which is an array of straight channels of 600 μm width were separately fabricated as described in section 2.3, using PDMS. A PDMS membrane of 40 μm thick was fabricated by spin coating PDMS with a 1:5 ratio of curing agent to base onto a 30 μm thick Mylar sheet. The open side of the wells in the storage layer was plasma-bonded to this membrane. Then the Mylar sheet was peeled off from the other side of the membrane and plasma-bonded to the open side of the channels in the reservoir layer. For the structural support along with the X-ray transparency, the chips were sealed, by bonding 8 μm thick Kapton foil to the sides of storage and reservoir. Figure 5.2(b) shows the cross section of the effective X-ray semi-transparent device and Figure 5.2(c) show the final assembled device with a thick PDMS bonded to one of the Kapton foil for the chip-to-world interfacing, with a window cut out in the region where the X-ray diffraction would take place.

We primed the chip by dead-end filling the aqueous reservoir with a 1.5 M $NaCl$/1.5 M $(NH_4)_2CO_3$ solution as the CO_2 and the NH_3 source into a selected channel of the reservoir and with 12 wt% Fluorooctanol in FC-43 oil into the storage layer until no air-bubbles remained trapped in the chip. After priming the storage layer we injected 1 M $CaCl_2$ in order to create the drops inside the wells. The flow rate was kept at 100 $\mu L/hr$. After the resevoir channels got primes, the 1.5 M $NaCl$/1.5 M $(NH_4)_2CO_3$ solution was injected at 200 $\mu L/hr$ and continue to flush during the course of experiment, in order to continuously supply CO_2 and the NH_3 to the drops for the full consumption of the Calcium ions.

The pH of the 1.5 M $NaCl$/1.5 M $(NH_4)_2CO_3$ solution was kept at 9. A higher pH is needed because low pH starts to dissolve the $CaCO_3$ precipitants. Changing the pH of ammonium carbonate solutions will change the ratio of CO_2/NH_3 gas, with lower pH favoring more CO_2, but it will also add more ions and change the osmolarity so keeping the

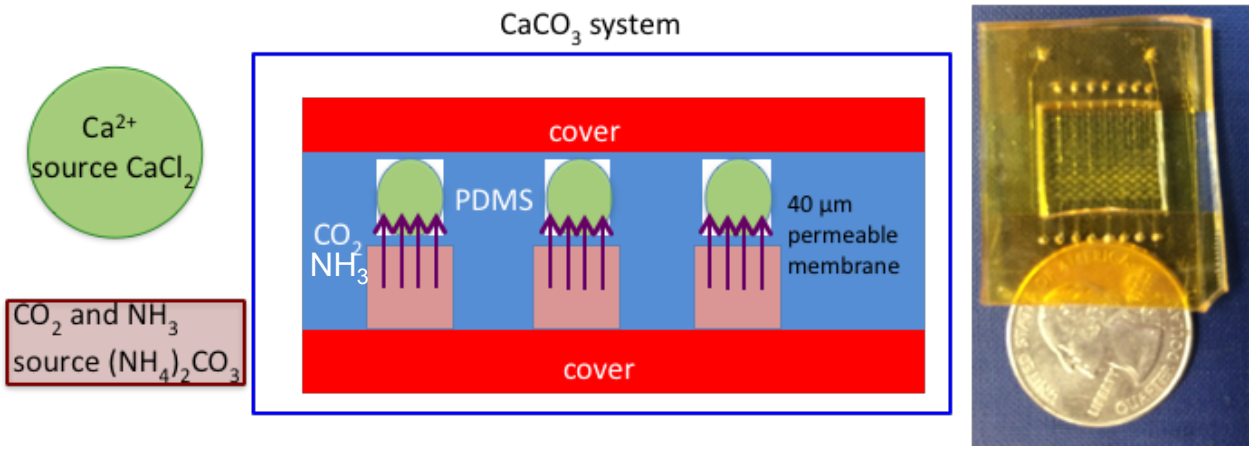

Figure 5.2: (a)The green circle indicated the Calcium source stored in the storage layer of the device as aqueous drops stabilized in surfactant.The red rectangle indicated the CO_2 and the NH_3 source running in the straight channels of the reservoir.(b) The cross section of the X-ray semi-transparent part of the device show the storage layer holding the drops of Calcium source and reservoir layer holding the CO_2 and the NH_3 source, separated by a 40 μ thick permeable membrane. The upward arrows indicate CO_2 and the NH_3 permeating thought he mebrane from the reservoir to the storage drops. The cover is the 8 μm thick Kapton foil. (c) The assembled decive along with a US quarter for size comparision

pH at exactly 9 is not crucial. $NaCl$ is used to match the osmolarity of the $CaCl_2$, so that the water chemical potential is flat across the membrane.

5.3 Formation of ACC and the transition to stable polymophs

We started recording time lapsed video before introducing the 1.5 M $NaCl$/1.5 M $(NH_4)_2CO_3$ solution to a particular channel in order to observe the early stages of ACC formation, in bright field microscopy with 4X objective. The drops started off with a clear solution and turned dark when the ACC formation begins. After about 20 mins the drops again start

to clear out because one or two nucleation cites of the stable polymoph started to consume the ACC and concentrate all the $CaCO_3$ into the crystal. Figure 5.2(a) shows the instantaneous images of the time lapsed movies at given time steps. Figure 5.2(b) shows one drop after ACC formation at a higher magnification. The stable polymorph could be vaterite, araganite, calcite or a mixture of them. With1.5 M $NaCl$/1.5 M $(NH_4)_2CO_3$ solution in the reservoir channel, we consistently observe the ACC formation within 2 - 3 mins since we introduce the solution. The stable polymorph begins to grow after about 20 mins from the time of introducing the solution and consumes all the ACC available within 30 mins. In the attempt of slowing down the formation of ACC for an efficient acquisition, we carried out experiments with 0.15 M $NaCl$/0.15 M $(NH_4)_2CO_3$ solution in the reservoir channel. We observed that the ACC formation was lagged down to 5 - 6 mins from the time of introducing the solution and the stable polymorph consumes all the available ACC within 90 mins from time of introducing the solution.

5.4 X-ray diffraction

We made X-ray semi-transparent version of the permeable PhaseChip for the first time for this application and hence we carried out a regular wide angle X-ray scattering experiment with the $CaCO_3$ system with synchrotron radiation as a proof of principle. X-ray diffraction data were collected at Cornell High Energy Synchrotron Source (CHESS), beamline F1 (λ = 0.9179 Å, E = 13.508 keV, X-ray flux = 5.53 * 10^{10} photons/sec), using a 100 μm monochromatic X-ray beam from a 24-pole wiggler. The chips were mounted at a distance of 200 mm from an Area Detector Systems Corporation (ADSC) Quantum 270 (Q270) detector, corresponding to a largest inscribed circle of resolution of 1.4 Å. The detector face was oriented perpendicular to the beam. Data sets were collected at room temperature

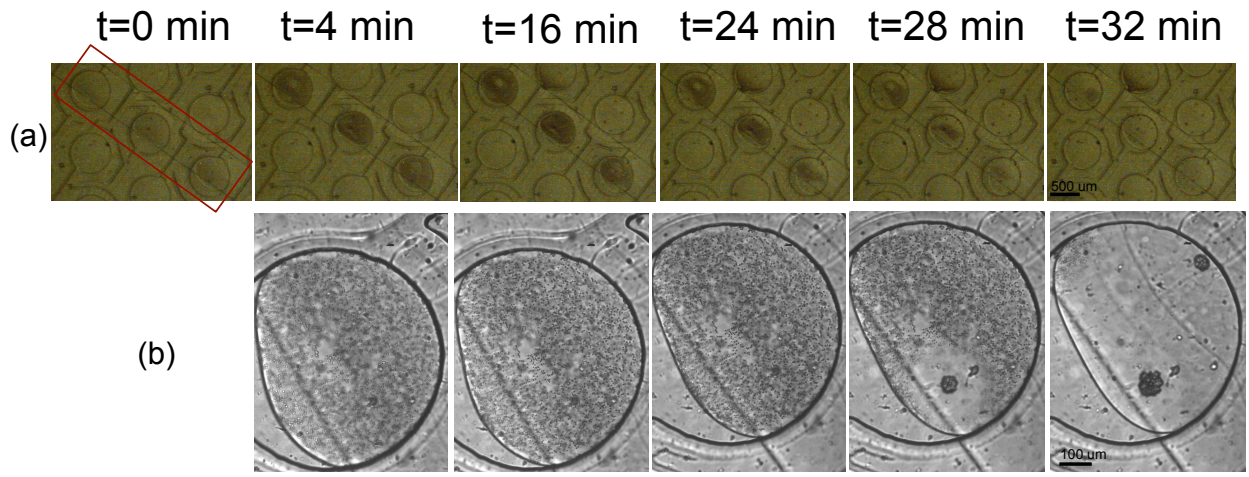

Figure 5.3: (a) Time series images for the formation of ACC from solution and transitioning to stable polymorphs such as vaterite and calcite. The diagonally place rectangle is for the visual guide of the 3 drops which are picked for observation and the reservoir channel running underneath them.(b) One drop under the observation with 20x objective after formation of ACC which undergo the transition into a stable polymorph.

(∼25°C). The X-ray semi-transparent chip mounted on the goniometer inside the Cornell CHESS F1 beamline, shown as Figure 2.4. In addition, the inlet tubing was connected to a programmable syringe pump with a flow rate of 200 $\mu L/hr$ for the reservoir solution and the outlet was connected to a waste line. We used 1.5 M $NaCl$/1.5 M $(NH_4)_2CO_3$ as the reservoir solution and 1 M $CaCl_2$ solution in the storage drops.

As of the original experiment plan, attempts were made to collect SAXS data for the early evolution of ACC, at the DND-CAT beamline of Advanced Photon Source (APS) at Argonne national laboratory. X-ray scattering from microfluidic chips with and without aqueous sample and precipitates has been evaluated. Due to the difficulty locating storage wells without a high-resolution camera, the exact contributions to the scattering from individual components (kapton, PDMS, COC, water, precipitate, etc.) were difficult to quantify. At the beamline, the general region of the wells was located optically, and then an attempt was made to focus the beam at the center of the well by obtaining symmetric scattering

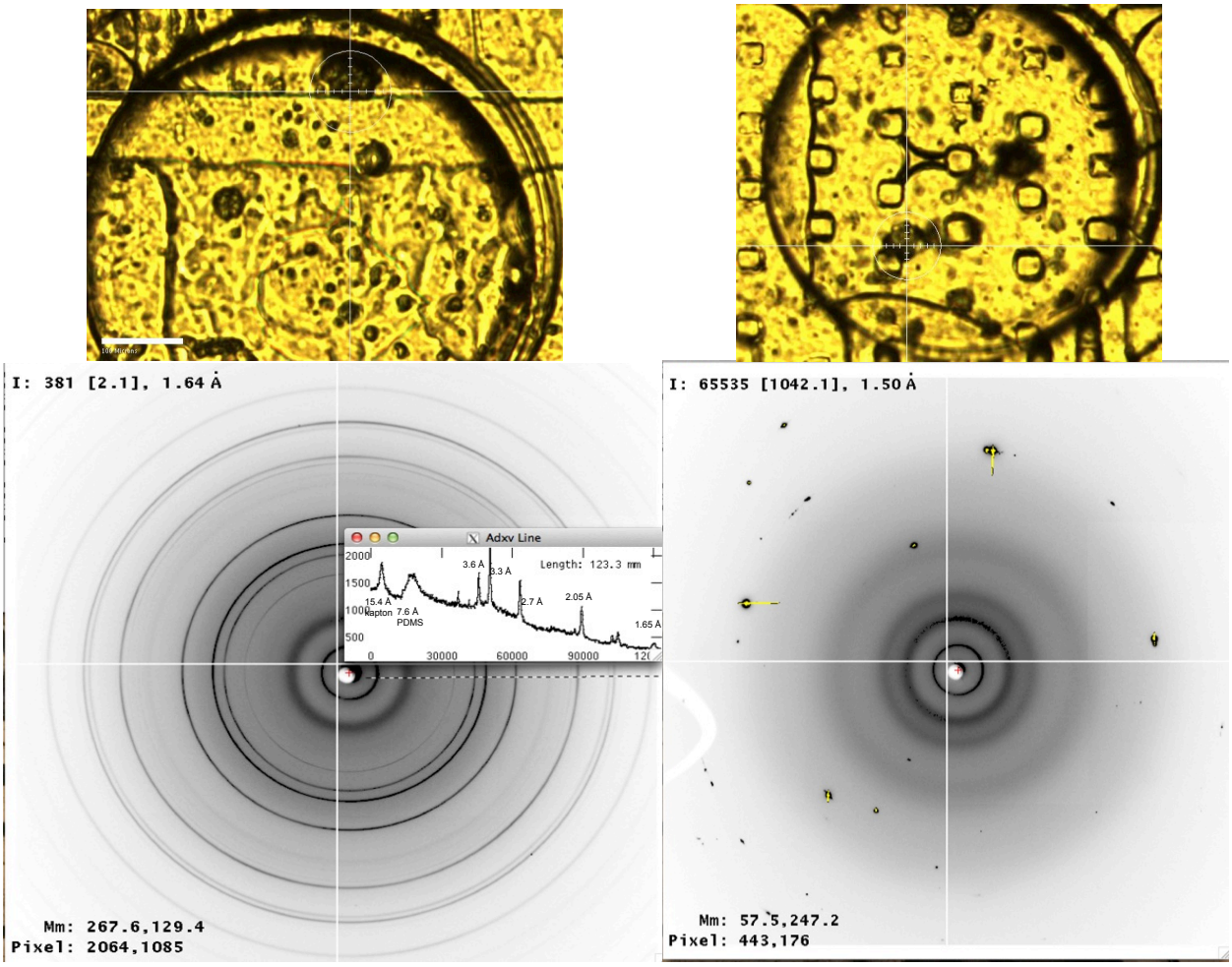

Figure 5.4: The two X-ray diffraction images show the diffraction pattern of the corresponding stable morphologies imaged by the bright field camera at the beam, place directly above them. The Line Window tool of AADXV [**?**] overlaid on the right hand side diffraction image displays the peaks corresponds to the device materials; PDMS and Kapton which are in the low resolution region

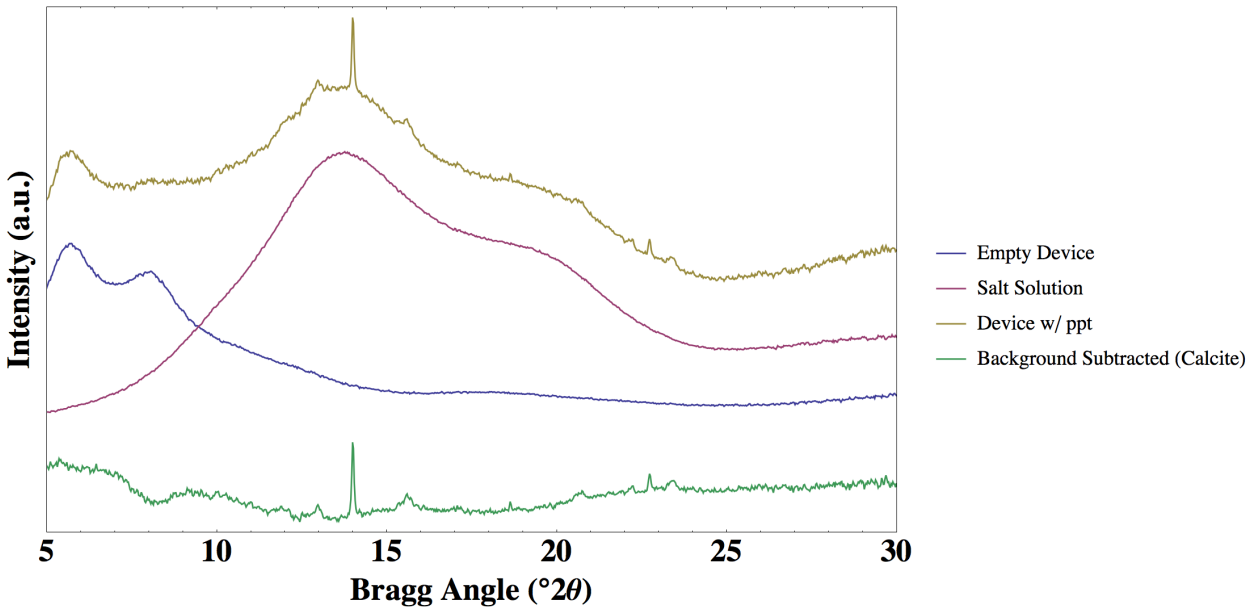

Figure 5.5: WAXS of empty device (blue), bulk salt solution simulating aqueous contents of device (red), a device 30 minutes after starting ammonium carbonate flow containing calcite crystals unprocessed (yellow), and with the contributions from background signal removed (green).

in SAXS, presumably from the circular walls of the well. The channels beneath the wells, which were not perfectly centered and produced a distinct scattering signal, complicated this process. Therefore, we can only qualitatively assess the contributions to scattering from the microfluidic devices and their aqueous and solid contents.

We were not able to obtain time-resolved scattering data during the course of precipitation. Precipitates were only found after searching a device in which ammonium carbonate had been introduced for 30 min. Any amorphous material that initially precipitated had crystallized, producing easily identifiable Bragg peaks in Wide Angle X-ray Scattering (WAXS) Figure 5.5. However, this was not necessarily due to the inability to resolve an ACC scattering signal. We know from independent experiments that the growth of ACC particles precipitated under similar reagent concentrations is easily observed as an increase

in SAXS intensity by 3 orders of magnitude, but it was not feasible to use this signature as an instantaneous landmark for the wells while the reaction was underway. This highlights the importance of using a camera or fiber-optic microscope to focus the beam on the area of interest.

5.5 Conclusion

We successfully fabricated the X-ray semi-transparent version of the PhaseChip first time and tested on Calcium Carbonate crystallization. Microfluidically made emulsion drops of calcium ions stored in a this device were systematically exposed to CO_2 and NH_3 permeated through a PDMS membrane from a reservoir to trigger the ACC formation. Although we couldn't successfully determine the mechanism of ACC formation due to the technical difficulties at the SAXS beamline, we successfully controlled the lag time of ACC formation since we introduce the reservoir solution, by changing the concentration of the reservoir solution. The change on the concentration of the reservoir solution also changed the transition time of the stable polymorphs. Transition times goes up to three folds when we reduce the concentration of reservoir solution by 10 folds. The effects of the drop size, membrane thickness and additive concentration are interesting parameters of ACC formation, that can be easily and robustly investigated using this technology. For successful SAXS experiments on resolving the mechanism of ACC formation demands optimization of the concentration of $NaCl/(NH_4)_2CO_3$ along with the other parameters such as acquisition time of the detector with a better camera at the beamline. Along this route, we could also envision fabricating X-ray semi-transparent dialysis PhaseChip [38] for membrane protein crystallization and X-ray diffraction.

5.6 Acknowledgement

We thank Frank Mello from the Brandeis Machine Shop for fabricating the stainless steel magnet adapter, and Irina Kriksunov, Richard Gillilan, David Schuller, Mike Cook, and Scott Smith for discussions and help setting up the microfluidics devices at F1 beamline at CHESS, and Steve Weigand for the useful discussion and help at APS facility.

Chapter 6

Conclusion and Future direction

This Dissertation elaborates the technology building projects in the advancement of microfluidics along the areas of X-ray diffraction and sample delivery systems in synchrotron and Free electron laser facilities to aid protein crystallization and biomineralization. Simultaneous to these technology developments, we have addressed the fundamental questions of; kinetic optimization of crystal nucleation and growth essential for X-ray diffraction, non-Poisson nature of nucleation via evaporation and stabilization of amorphous calcium carbonate in microfluidic confinement as precursors for the stable polymorphs. We presented a technology that optimizes the kinetics of crystallization, eliminates crystal handling, eliminates cryoprotection and simplifies collection of diffraction data for structural biology. This technology is based on crystalizing protein in surfactant stabilized emulsion drops of ideal size to grow a single crystal confined in X-ray semi-transparent microfluidic devices. As a proof of principle, the structure of Glucose Isomerase was solved and refined at 2.09 Å resolution, to an R_{cryst}/R_{free} of 0.144/0.174, using merged diffraction datasets from 72 crystals of about 50 μm by 40 μm by 30 μm in size. We studied the non-Poisson nucleation of protein crystals nucleated and grown in a simple and robust X-ray semi transparent microfluidic device, in-

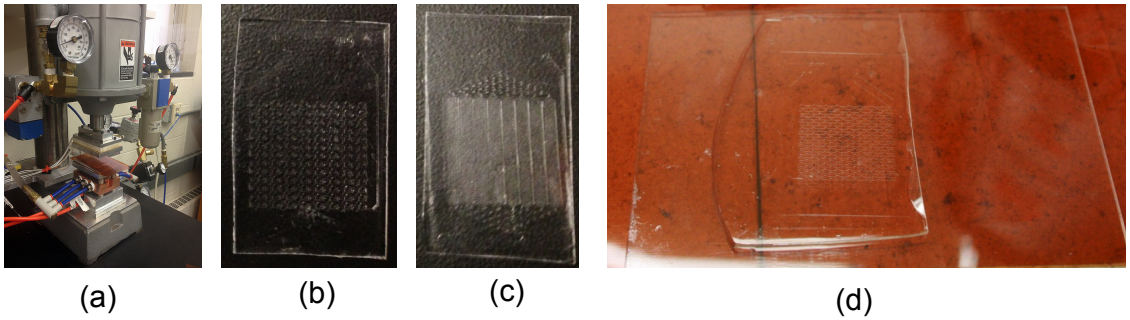

Figure 6.1: The thermal press which is used for embossing thermoplastics. (b) and (c) are the storage and reservoir layers of PhaseChip embossed on150 μm thick COC sheets (TOPAS) (d) The PDMS master used for the embossing

tegrated with controlled evaporation. We exploited the inherent nature of the high water permeability of the thin X-ray semi-transparent devices to create homogenous and heterogeneous evaporation rate profiles over the device and hence manipulated the phase space by increasing the supersaturation of the protein. We have fabricated a series of wafer and transmission electron microscopy (TEM)-style grid supports constructed of low-Z plastic as fix target supports for the the sample delivery systems in X-ray free electron lasers (XFELs). Finally, for the first time we successfully fabricated the X-ray semi-transparent version of the PhasChip, which comprised of two thin patterned PDMS layers separated by another thin PDMS membrane which facilitate water and gas permeability. We employed this technology to investigate the formation of amorphous calcium carbonate and it's transitioning into more stable polymorphs, using X-ray diffraction.

In the attempts of improving the X-ray transparent microfluidics technologies, the material selection and fabrication methods play a major role. Current fabrication method suffers from bonding featured PDMS to thin foil lids via silane chemical coupling, which is the bottleneck of mass production for industrial scale. This problem can be solved by employing Rapid prototyping methods of thermoplastics, which is an emergent field along with the

use of the current toolbox Figure 6.1. Among the variety of thermoplastics, Cyclo olefen coppolymer (COC) shows promising future in microfluid device fabrication due to it's bio-compatibility, hydrophobicity and better optical properties. Thermal embossing the features onto thin COC and using it as the lidding material would benefit the fabrication process of X-ray semi-transparent microfluidics device in many folds.

Appendix A

One Crystal per Drop: Theory and Simulation

This appendix is adapted from the appendix to [39] which is originally published in *IUCrJ*.

In this section we calculate the drop volume such that only one crystal is nucleated per drop. Consider a drop that contains a supersaturated solution that has not nucleated any crystals. As long as the physical-chemical environment is constant, the nucleation rate, J [# of crystals per unit volume, V, and per unit time, t], will also be constant and the probability, P, of nucleating a crystal in a drop of volume V in an infinitesimal time interval τ is independent of the time, t,

$$P(t, t+\tau) = JV\tau, \tag{A.1}$$

from which it follows that the probability that a drop has not nucleated any crystals is $p(t) = e^{-JVt}$. If, by some contrivance, each drop could only produce one crystal, then since the probability of not crystallizing and the probability of crystallizing have to add to one,

we have an expression for the average number of crystals per drop as a function of time;

$$x(t) = 1 - e^{-JVt}. \tag{A.2}$$

However, once a drop does nucleate a crystal, the nucleation rate is reduced due to the growing crystal consuming protein in solution and nucleation ceases to be a Poisson process, which makes finding an analytical solution to the number of crystals per drop as a function of time a difficult problem [18, 32].

To address the question of how many crystals nucleate per drop as a function of drop size, we developed a Monte Carlo simulation in one dimension, a special case for which the drop size and volume are equal. Our approach differs from that taken previously by Dombromski [18] in that our model explicitly calculates the spatial-temporal concentration profile within the drop. Drops were modeled as a lattice of points, where each point was characterized by two quantities; the protein number concentration, $c(x,t)$ [L^{-3}], and a binary indicator that signified whether the protein was in a crystalline or solution state. The protein was confined in the drop, meaning that no-flux boundary conditions were imposed on the ends of the lattice. The numerical values used in the model, while within an order of magnitude of values used in our experiments, were not reflective of any particular protein or physical set of conditions. Rather they were chosen for two purposes. First, to satisfy the assumptions of the theory, i.e. that the rate of crystal growth was much larger than the rate of nucleation. Second, to ensure that the simulations were quick to perform. Thus the diffusion constants and nucleation rates were chosen to be higher than actual values. This means that the simulations were faster to perform, but that they conclusions were not affected as they depend on the ratio of the diffusion rate to nucleation rate and not on their absolute values. Protein concentrations in solution evolved according to the diffusion

equation; $\delta c/\delta t = -D\nabla^2 c(t)$, with $D = 6 \times 10^{-10}$ [$\mathrm{m^2 s^{-1}}$], the protein diffusion constant. Initially the drop was homogeneous in protein number concentration, $c = 1$ $\mu\mathrm{m}^{-3}$, at a high value of supersaturation, $s = 83.3$, with $s = c/c_s$, with $c_s = 0.012$ $\mu\mathrm{m}^{-3}$, the concentration of the saturated protein solution in equilibrium with the protein crystal, and with $l = 1$ μm, the size of a lattice site. At each time step, there was a finite probability that a randomly chosen lattice site could transform into a crystal with a probability, P, given by $P = Jl^3\tau$ and $\tau = l^2/D$ the simulation time step. In the simulation we used the classical nucleation theory expression for nucleation rate, $J = sAe^{-B/\ln(s)^2}$ [27], where A and B are constants such that $P = sR\ 666e^{-350/\ln(s)^2}$, with R a dimensionless rate coefficient. The protein concentration of a lattice site coinciding with the edge of a crystal was increased at a rate proportional to the supersaturation according to $\delta c/\delta t = v(c(t) - c_s)/l$, where $v = 1 \times 10^{-3}$ [$\mathrm{ms^{-1}}$] is the constant velocity of crystal growth [78, 14]. Conservation of mass was used at the boundary between the crystal and solution. The concentration per lattice site in a growing crystal was limited to an arbitrary value of $c_{\mathrm{xtal}} = 4$ to model the effect that protein crystals have a fixed density that is of order 100 c_s. Once a lattice site exceeded this maximum concentration, the crystal would grow symmetrically, one lattice site to the right and to the left. It was assumed that crystals were stationary once nucleated.

Figures B.1(A) and B.1(B) show the simulation results. Parameters were chosen to approximate our experiments; high supersaturation, fast growth, and drops of order 100 μm diameter. In each case, the simulation begins by instantly quenching the drop to a supersaturation of 83. The two figures are taken after nucleation has occurred, but before equilibrium is achieved. In Figure B.1(A), the nucleation rate is low, $R = 1$ in dimensionless units. In what follows, time, t, is non-dimensionalized by $\tau = l^2/D$, and distance is nondimensionalized by $l = 1$ μm. The red dashed line indicates the initial condition, at $c = 1$, while Figure B.1(A) occurs at $t = 250$. The crystal that nucleated first is centered at $l = 19$. The

width of the crystal increases as protein from solution is fed into the crystal. Later a second crystal is independently nucleated. The growing crystals deplete the protein concentration in the region bordering the crystals. In equilibrium the protein concentration remaining in solution will be homogeneous and equal to the saturation concentration. Figure B.1(B) differs from the conditions of Figure B.1(A) in that the dimensionless nucleation rate is higher, $R = 27$. More crystals are formed, even though the duration of the quench at which Figure B.1(B) is recorded, $t = 50$, is less than in Figure B.1(A). The protein in solution has obtained the equilibrium value in between the two rightmost crystals. A noteworthy observation is the development of a depletion zone in the neighborhood of each growing crystal. If the local concentration is reduced sufficiently, then no additional crystals will nucleate in the depletion zone. The size of the depletion zone is different between the two figures; therefore the depletion zone is a function of the nucleation rate J.

Figure B.1(C) shows the average number of crystals per drop as a function of time obtained from the simulation and compared with a fit to

$$\langle x(t) \rangle = x_\infty \left(1 - e^{-kt}\right). \tag{A.3}$$

The simulation conditions were identical to the conditions of Figures B.1(A) and B.1(B); a drop size of 60 μm, and two nucleation rates, $R = 27$ and $R = 1$. The simulation and fit to Equation A.3 overlap completely. Equation A.2 has two fitting parameters, x_∞, the final number of crystals per drop and k, the non-dimensional rate at which crystals form. Figure B.1(D) shows how the final number of crystals per drop varies a function of drop size for two nucleation rates, $R = 27$ and $R = 1$, while Figure B.1(E) shows how the dimensionless rate, k, varies with size.

Figures B.1(A) and B.1(B) of the concentration profile inside a supersaturated drop of

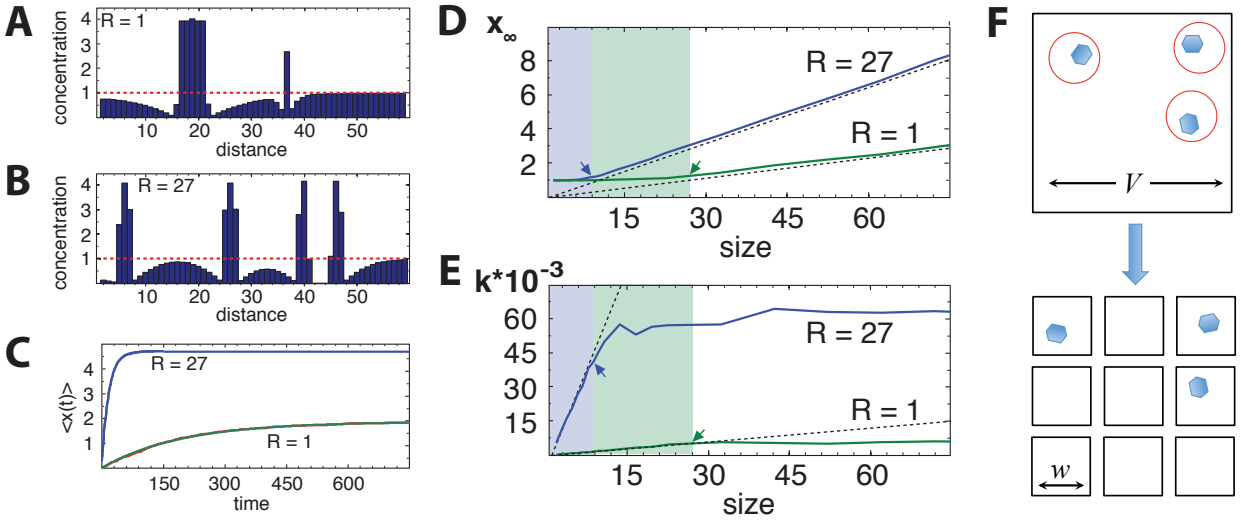

Figure A.1: (A and B) Protein concentration as a function of distance from a simulation of nucleation and growth in one dimension. Concentration is dimensionless. Red dotted line indicates the initial concentration with a supersaturation of 83.3 at $t = 0$. The sites with concentrations that exceed the red line are in the crystalline phase, while those below are in solution. (A) Concentration profile at $t = 250$. Slow nucleation rate of $R = 1$ in dimensionless units. (B) Concentration profile at $t = 50$. Fast nucleation rate of $R = 27$. (C) Average number of crystals per drop as a function of time, $\langle x(t) \rangle$, for two nucleation rates obtained from simulation and fitted to Equation A.3, $\langle x(t) \rangle = x_\infty \left(1 - e^{-kt}\right)$. Conditions are the same as in (A) and (B). (D and E) Fitting parameters to Equation A.3 as a function of drop size for two nucleation rates, $R = 27$ and $R = 1$. Arrows indicate size of depletion zone. (D) The solid lines are the simulated final number of crystals per drop, x_∞. Dashed lines are Equation A.7, $x_\infty = V/w^d$. (E) The solid lines are the simulated rate of crystal formation, k. Dashed lines are Equation A.8, $k = JV$. (F) Conceptual schematic. A drop of volume V can be thought of as x_∞ smaller, independent drops of volume $w^d = V/x_\infty$

protein solution during crystallization are suggestive of a depletion zone in the vicinity of a growing crystal in which the supersaturation is reduced sufficiently such that no new crystals can be nucleated. Let w be the width of this depletion zone and let τ be the time interval for which the average number of crystals nucleated in a volume w^d, is one, where d is the spatial dimension. Then, from Equation A.1 it follows

$$Jw^d\tau = 1, \tag{A.4}$$

which provides one equation relating the depletion zone to the nucleation time. In order for no additional crystals to nucleate in the depletion zone, the protein in solution must be able to diffuse through the depletion zone to the growing crystal, thereby lowering the supersaturation in the depletion zone, in less than the depletion time. This provides a second equation between the depletion zone and nucleation time,

$$\tau = \frac{w^2}{D}. \tag{A.5}$$

To be self-consistent, we combine Equations A.4 and A.5, which yields

$$w^{d+2} = \frac{D}{J}. \tag{A.6}$$

Figure B.1(D) shows the simulated dependence of the number of crystals per drop, x_∞, as a function of drop size in one dimension, $d = 1$, for which $w = (D/J)^{1/3}$. Examine the curve with the higher nucleation rate, $R = 27$. For small drops, less than drop size ~ 9, the number of crystals per drop remains constant at $x_\infty = 1$. "Small" means $V < w^d$, i.e. the time for protein to diffuse the entire length of the drop is less than the nucleation time, so that after one crystal has been nucleated, its growth causes a negative feedback suppressing

further nucleation throughout the entire drop. As the size of the drop is increased beyond the depletion zone, w, x_∞ becomes greater than one and the number of crystals per drop grows linearly with drop size. Each nucleation event produces a new depletion zone with just one crystal inside. This process repeats until the entire drop is filled with crystals, each occupying a part of the drop equal to the depletion zone, w. This scenario predicts that the number of crystals per drop is

$$x_\infty = \frac{V}{w^d} = V\left(\frac{J}{D}\right)^{\frac{d}{d+2}}. \tag{A.7}$$

The dashed lines in Figure B.1(D) show this behavior; the lines start at the origin and have slope $1/w$. The ratio of nucleation rates in the two examples shown in Figure B.1(D) is 27, and as $1/w \propto J^{1/3}$, the prediction is that the ratio of the slopes of the dashed lines in Figure B.1(D) is 3, as observed. Furthermore, the width of the depletion zone scales as $w \propto J^{-1/3}$. Thus for the drop in Figure B.1(D) with slow nucleation rate $R = 1$, the width of the depletion zone, manifested by the drop size for which x_∞ first becomes greater than one, is predicted to be three times greater than the depletion zone of the drop with the fast nucleation rate $R = 27$, as observed in Figure B.1(D).

As the drop volume, V, is increased from zero, the rate, k, of nucleating one crystal in V will increase linearly with drop volume as predicted by Equation A.1 for Poisson processes

$$k_v = \frac{1}{\tau} = JV \tag{A.8}$$

the behavior seen in Figure B.1(E). However, once the drop volume exceeds the volume of the depletion zone, a crystal will be nucleated somewhere else in the drop; therefore the

frequency at which depletion zones are created is

$$k = \frac{1}{\tau} = Jw^d = J^{\frac{2}{d+2}} D^{\frac{d}{d+2}}. \tag{A.9}$$

Equations A.6 and A.9 predict that $k \propto J^{2/3}$ in one dimension and that k becomes independent of drop size V, as also seen in Figure B.1(E).

The picture that emerges from these simulations and dimensional analysis suggest that nucleation of multiple crystals in a drop is a Poisson process. This is an unexpected result as the nucleation rate is not constant: once the first crystal has nucleated, its growth acts to suppress further nucleation. However, we argue that each nucleation event creates a depletion zone in which it is only possible for one crystal to exist. Therefore, each nucleation event is an independent process. In effect, each drop can be thought of as being partitioned into x_∞ smaller, independent drops of volume $w^d = V/x_\infty$ that nucleate with rate k (Figure B.1 F). This justifies Equation A.3, and explains why in Figure B.1(C), the number of crystals per drop as a function of time is an exponential, a result indicative of a Poisson process.

The degree to which growing crystals create depletion zones is expected to be greatest in one dimension. For example, in one dimension no protein can be replenished in the gap between two crystals, while in higher dimensions, protein will diffuse into the gap between crystals along the directions perpendicular to the line connecting the centers of the crystals. Nevertheless, we expect the same general trends observed in 1D to carry over to 2D and 3D. In particular, in dimension d we expect there will be a drop volume $V_d \sim (D/J)^{\frac{d}{d+2}}$, below which only one crystal will be nucleated per drop.

The question of how many crystals will form per drop has been addressed theoretically and experimentally in several works. Our work is closest in spirit and results to that of Dombrowski et. al.[18] in that we both assume that a single crystal per drop results from

a competition between nucleation and growth rates. The differences are that our model explicitly treats spatial concentration variations and assumes that the crystal growth is diffusion limited. In contrast, Dombrowski et. al. [18] assume that the velocity of crystal growth is the rate limiting step. Then, as the crystal slowly grows, the concentration in the drop remains uniform, but decreases with time, eventually shutting off nucleation. In our experiments, we used high supersaturation in order to have a significant probability of nucleating a crystal in drops whose volume is less than a nanoliter. This leads to a fast growth rate in which diffusion of protein from solution to the crystal is limiting the rate of growth. Experimental measurements of the number of crystals per drop as a function of drop size agree with our model [55, 4]. Another theory [56] balances the rate of crystal growth with the diffusive flux of protein in order to identify a critical size for obtaining one crystal per drop. Their theory leaves out the key physics of balancing nucleation and growth and disagrees with our model, simulations and experiments [4].

Appendix B

X-ray diffraction data and electron density map

This appendix shows the X-ray diffraction data collected at Petra III, P14 beam line using the crystals grew in X-ray semi-transparent PhaseChip devices via controlled evaporation.

SUBSET OF INTENSITY DATA WITH SIGNAL/NOISE >= -3.0 AS FUNCTION OF RESOLUTION

RESOLUTION LIMIT	NUMBER OF REFLECTIONS OBSERVED	UNIQUE	POSSIBLE	COMPLETENESS OF DATA	R-FACTOR observed	R-FACTOR expected	COMPARED	I/SIGMA	R-meas	CC(1/2)	Anomal Corr	SigAno	Nano
7.83	5629	611	615	99.3%	18.6%	16.1%	5605	13.25	19.9%	94.6*	-3	0.847	373
5.53	11711	1067	1067	100.0%	17.8%	17.4%	11697	13.25	18.7%	93.9*	5	0.865	785
4.52	15740	1324	1328	99.7%	17.6%	17.1%	15733	14.19	18.4%	96.8*	-7	0.832	1050
3.91	18869	1560	1567	99.6%	18.1%	17.3%	18861	14.33	18.8%	97.4*	0	0.870	1271
3.50	21624	1769	1774	99.7%	17.9%	17.8%	21612	13.68	18.7%	97.3*	1	0.869	1473
3.20	24359	1952	1953	99.9%	18.5%	18.9%	24347	12.66	19.4%	96.2*	1	0.850	1628
2.96	26268	2090	2093	99.9%	20.0%	20.8%	26258	11.31	20.8%	97.3*	-1	0.832	1759
2.77	27935	2242	2246	99.8%	21.6%	22.5%	27929	10.25	22.5%	96.9*	-1	0.844	1880
2.61	28796	2405	2405	100.0%	23.6%	24.4%	28781	9.30	24.6%	95.8*	-2	0.858	2012
2.48	31290	2533	2534	100.0%	26.3%	27.1%	31273	8.48	27.4%	95.6*	1	0.885	2143
2.36	32420	2626	2627	100.0%	27.4%	28.1%	32407	8.07	28.6%	95.8*	-3	0.855	2252
2.26	34268	2776	2776	100.0%	30.2%	30.9%	34259	7.33	31.6%	94.9*	2	0.883	2435
2.17	35202	2878	2879	100.0%	32.7%	33.2%	35192	6.84	34.1%	92.5*	-2	0.856	2492
2.09	36851	2994	2999	99.8%	35.9%	37.2%	36840	6.08	37.4%	93.3*	-1	0.849	2615
2.02	37467	3095	3098	99.9%	41.2%	42.8%	37454	5.19	43.1%	91.4*	-3	0.849	2682
1.96	38131	3190	3195	99.8%	46.7%	48.6%	38111	4.51	48.8%	89.7*	-2	0.826	2749
1.90	38357	3277	3283	99.8%	53.5%	56.3%	38330	3.89	55.9%	86.6*	-2	0.828	2812
1.84	39650	3421	3422	100.0%	64.8%	69.7%	39632	3.07	67.8%	84.1*	-2	0.767	2922
1.80	33575	3465	3476	99.7%	72.3%	79.1%	33537	2.45	76.3%	82.2*	-1	0.739	2760
1.75	19109	3114	3562	87.4%	72.3%	79.2%	18760	1.86	78.2%	69.1*	4	0.765	1695
total	557251	48389	48899	99.0%	23.4%	23.6%	556618	7.24	24.5%	96.6*	-1	0.834	39788

Figure B.1: The initial data merging 49 of 84 crystals into a dataset, gives the stats down to 1.7-1.8 Angstrom

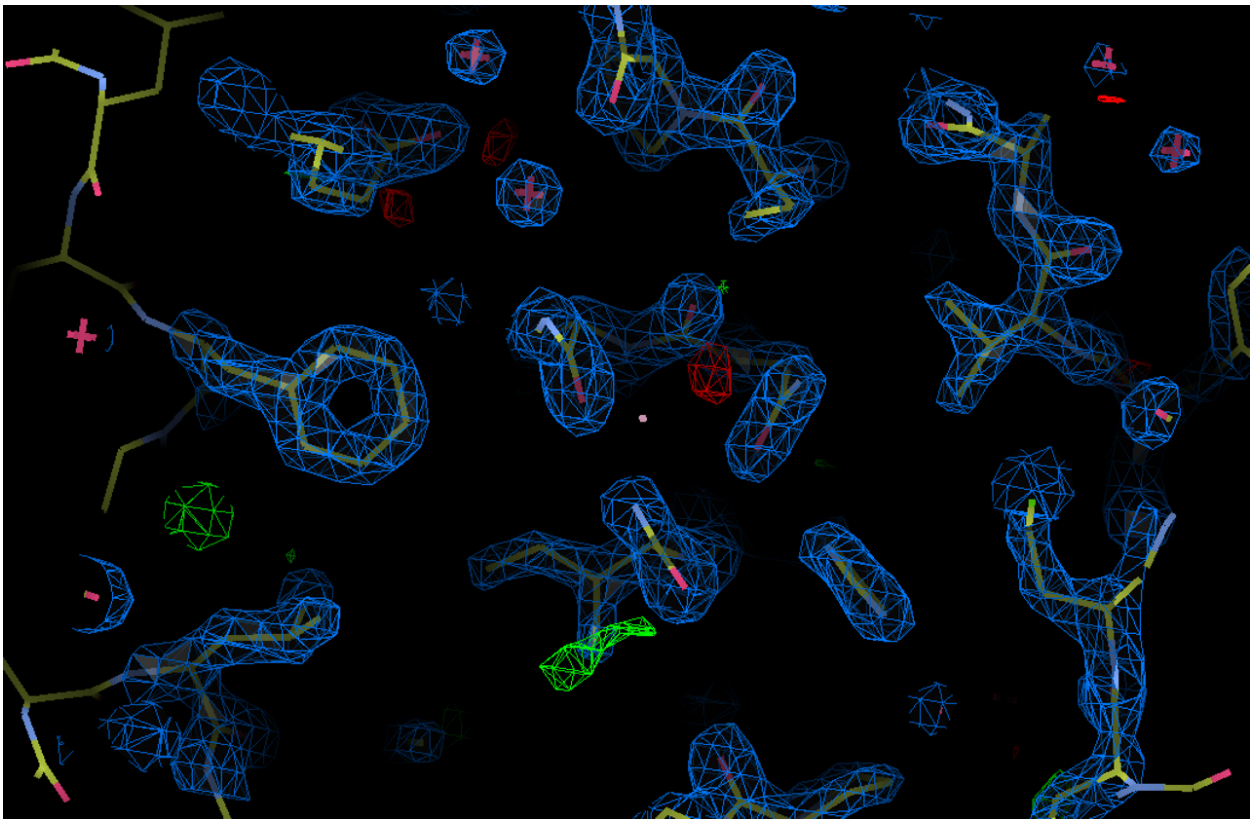

Figure B.2: Electron density map obtained with the above XRD data merged over 49 crystals along with the 8XIA pdb and molecular replacement with phenix in autopilot.

Appendix C

Xylose isomerase purification from *Thermus thermophilus*

This appendix describes the protein purification and crystallization steps for Xylose Isomerase from *Thermus thermophilus.* The complete expression and purification process was done with the supervision and guidance of Dr. Marc Ridilla, Director, Biological Materials Facility, Brandeis University Materials Research Science and Engineering Center.

Expression

A Thermus thermophilus xylose isomerase (XI) expression plasmid was ordered from the RIKEN BioResource Center. The plasmid contains the XI gene under the control of the T7 lac promoter and confers ampicillin resistance. DH5α and BL21(DE3) E. coli with it was transformed and stored the rest at -20°C . Liquid cultures of both clones were grown overnight in LB media (10 g/L tryptone, 5 g/L yeast extract, 10 g/L NaCl) with 100 μg/mL ampicillin and prepared 10 % (v/v) glycerol stocks, which were stored at -80°C that could

be used to inoculate future cultures.

An overnight starter culture of the BL21(DE3) clone in LB was diluted 1:200 into 4.5 L pre-warmed LB (9x500 mL flasks), and flasks were incubated until they reached an optical density at 600 nm (OD600) of 0.6, then expression was induced by adding 1 mM IPTG. The cultures were incubated an additional 6 hours while the protein was expressed, then the cells were harvested by centrifugation and stored at -80°C until we were ready to begin purification.

Purification

Frozen cells from 2.25 L culture (half the expression culture) were resuspended to about 15 mL in 100 mM Tris pH 7.2, 1 mM β-ME, protease inhibitors, and lysozyme. Lysis was completed by sonication. The lysate was heated to 85°C for 15 min to denature all the non-thermostable E. coli proteins, and the sample was clarified by centrifugation for an hour at 18,000xg.

Protein concentration in the sample was estimated as 146 mg/mL by 280 nm absorbance (Abs 0.1% (=1 mg/mL) 1.295). 10 mg was diluted to 20 mg/mL for analytical SEC on the Superdex 75 size-exclusion column in 50 mM Tris pH 7.2. The leading peak appeared pure and monodisperse, so SDS-PAGE was done to further assess purity.

Analysis of the gel image revealed 96 % purity, which we concluded was sufficient. The remaining (10-mL) sample) required two HiPrep 16/60 Sephacryl S-200 SEC runs, which were conducted overnight.

Note: If it had not been pure enough, we'd have loaded the entire sample on a HiTrap Q FF anion exchange column and eluted in a gradient from 0 to 500 mM NaCl. After that we would have needed to concentrate and SEC the pure XI again to get it into NaCl-free

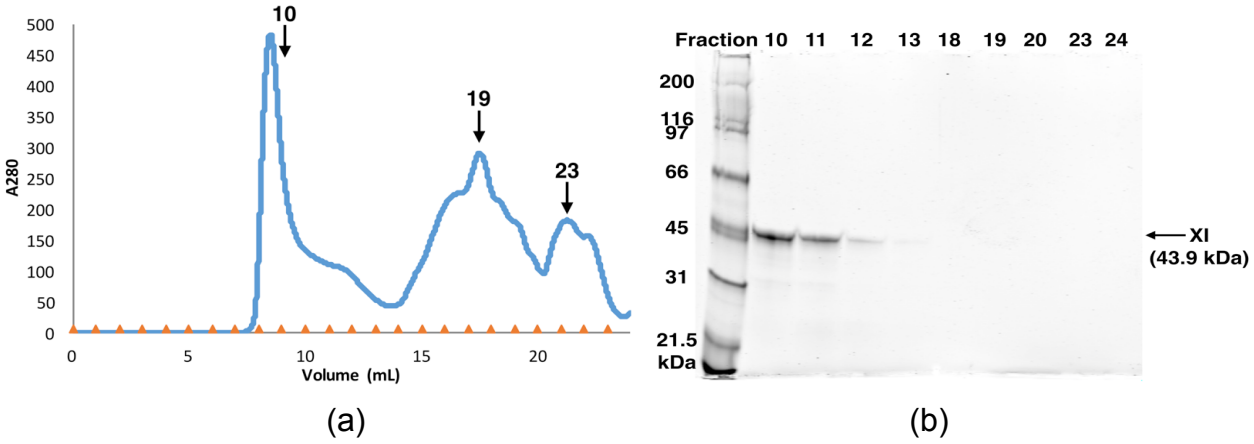

Figure C.1: (a)The absorption spectra of the fractions 0 - 25 (b) The SDS-PAGE gel image for the fractions 10 - 24

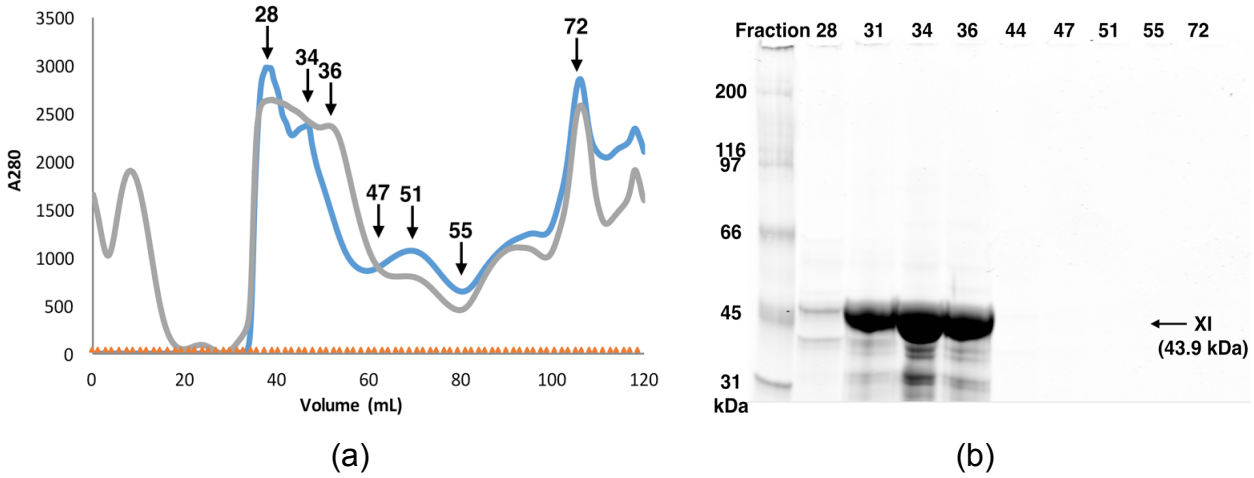

Figure C.2: (a)The absorption spectra of the fractions 0 - 120 (b) The SDS-PAGE gel image for the fractions 28 - 72

buffer.

Fractions 25-39 were pooled, yielding 45 mL at 7.388 mg/mL (332.5 mg total; 148 mg/L E. coli). The pure XI was concentrated to 135.352 mg/mL at 2.3 mL (311.3 mg total; 138 mg/L E. coli), then diluted back to 120 mg/mL for aliquoting. Aliquots were flash-frozen in liquid N2 and stored at -80°C.

A series of crystallization trials were carried out and 10 - 100 μm size crystals appeared

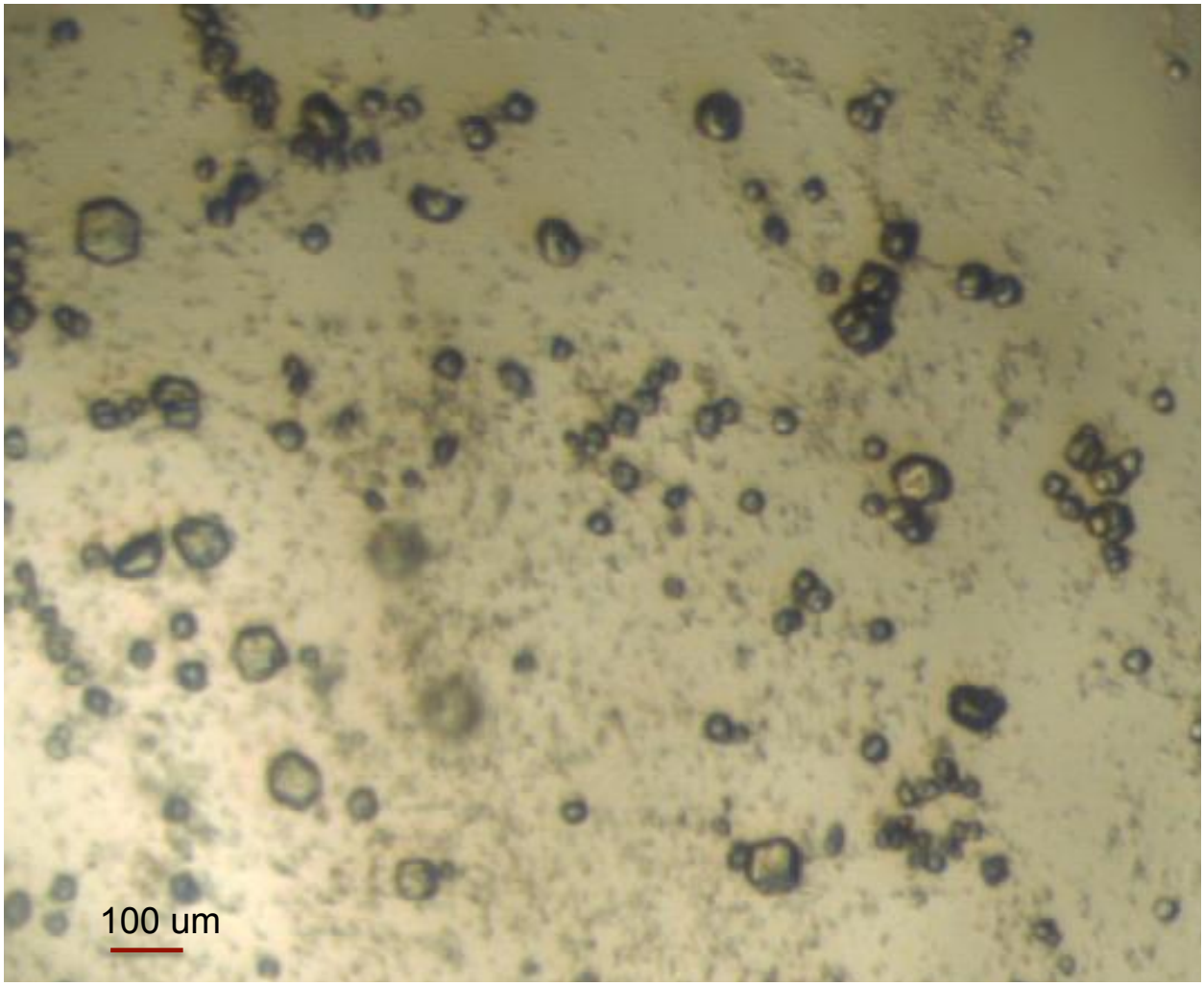

Figure C.3: 10 - 100 μm size XI crystals from *Thermus thermophilus*

in 2-3 days in the mixture of 13 %(w/v) PEG, 66 mM Ammonium Sulfate and 80 mg/ml XI in 33 mM Tris buffer in a total volume of 40 μl at room temperature, as shown in figure C.3.

Bibliography

[1] Priyanka D Abeyrathne, Mohamed Chami, Radosav S Pantelic, Kenneth N Goldie, and Henning Stahlberg, *Chapter one-preparation of 2d crystals of membrane proteins for high-resolution electron crystallography data collection*, Methods in enzymology **481** (2010), 25–43.

[2] L. Addadi, S. Raz, and S. Weiner, *Taking advantage of disorder: Amorphous calcium carbonate and its roles in biomineralization*, Advanced Materials **15** (2003), no. 12, 959–970.

[3] Adxv tool, http://www.scripps.edu/~arvai/adxv.html (2013).

[4] S. Akella, Ph.D. thesis, Brandeis University, 2014.

[5] Sathish V. Akella, Aaron Mowitz, Michael Heymann, and Seth Fraden, *Emulsion-based technique to measure protein crystal nucleation rates of lysozyme*, Crystal Growth & Design **14** (2014), no. 9, 4487–4509.

[6] Andrew Aquila, Mark S. Hunter, R. Bruce Doak, Richard A. Kirian, Petra Fromme, Thomas A. White, Jakob Andreasson, David Arnlund, Saša Bajt, Thomas R. M. Barends, Miriam Barthelmess, Michael J. Bogan, Christoph Bostedt, Hervé Bottin, John D. Bozek, Carl Caleman, Nicola Coppola, Jan Davidsson, Daniel P. DePonte, Veit Elser, Sascha W. Epp, Benjamin Erk, Holger Fleckenstein, Lutz Foucar, Matthias Frank, Raimund Fromme, Heinz Graafsma, Ingo Grotjohann, Lars Gumprecht, Janos Hajdu, Christina Y. Hampton, Andreas Hartmann, Robert Hartmann, Stefan Hau-Riege, Günter Hauser, Helmut Hirsemann, Peter Holl, James M. Holton, André Hömke, Linda Johansson, Nils Kimmel, Stephan Kassemeyer, Faton Krasniqi, Kai-Uwe Kühnel, Mengning Liang, Lukas Lomb, Erik Malmerberg, Stefano Marchesini, Andrew V. Martin, Filipe R.N.C. Maia, Marc Messerschmidt, Karol Nass, Christian Reich, Richard Neutze, Daniel Rolles, Benedikt Rudek, Artem Rudenko, Ilme Schlichting, Carlo Schmidt, Kevin E. Schmidt, Joachim Schulz, M. Marvin Seibert, Robert L. Shoeman, Raymond Sierra, Heike Soltau, Dmitri Starodub, Francesco Stellato, Stephan Stern, Lothar Strüder, Nicusor Timneanu, Joachim Ullrich, Xiaoyu Wang, Garth J. Williams, Georg Weidenspointner, Uwe Weierstall, Cornelia Wunderer, Anton Barty,

John C. H. Spence, and Henry N. Chapman, *Time-resolved protein nanocrystallography using an x-ray free-electron laser*, Opt. Express **20** (2012), no. 3, 2706–2716.

[7] Thomas R. M. Barends, Lutz Foucar, Sabine Botha, R. Bruce Doak, Robert L. Shoeman, Karol Nass, Jason E. Koglin, Garth J. Williams, Sébastien Boutet, Marc Messerschmidt, and Ilme Schlichting, *De novo protein crystal structure determination from x-ray free-electron laser data.*, Nature **505** (2014), no. 7482, 244 – 247.

[8] J Bolze, D Pontoni, M Ballauff, T Narayanan, and H Cölfen, *Time-resolved {SAXS} study of the effect of a double hydrophilic block-copolymer on the formation of caco3 from a supersaturated salt solution*, Journal of Colloid and Interface Science **277** (2004), no. 1, 84 – 94.

[9] H. Boukellal, S. Selimovic, J. Jia, G. Cristobal, and S. Fraden, *Simple, robust storage of drops and fluids in a microfluidic device*, Lab on a Chip **9** (2009), 331–8.

[10] S Boutet, L Lomb, GJ Williams, and TRM Barends, *High-Resolution Protein Structure Determination by Serial Femtosecond Crystallography*, Science **337** (2012), 362–4.

[11] Axel T. Brunger, *Free R value: a novel statistical quantity for assessing the accuracy of crystal structures*, Nature **355** (1992), 472–5.

[12] H. L. Carrel, Jenny P. Glusker, Vincent Burger, Franco Manfret, Denis Tritsch, and Jean-Francois Bielmann, *X-ray analysis of d-xylose isomerase at 1.9 a: Native enzyme in complex with substrate and with a mechanism-designed inactivator*, Proceedings of the National Academy of Sciences of the United States of America **86** (1989), no. 4440–4.

[13] Henry N Chapman, Petra Fromme, Anton Barty, Thomas A White, Richard A Kirian, Andrew Aquila, Mark S Hunter, Joachim Schulz, Daniel P DePonte, Uwe Weierstall, R Bruce Doak, Filipe R N C Maia, Andrew V Martin, Ilme Schlichting, Lukas Lomb, Nicola Coppola, Robert L Shoeman, Sascha W Epp, Robert Hartmann, Daniel Rolles, Artem Rudenko, Lutz Foucar, Nils Kimmel, Georg Weidenspointner, Peter Holl, Mengning Liang, Miriam Barthelmess, Carl Caleman, Sébastien Boutet, Michael J Bogan, Jacek Krzywinski, Christoph Bostedt, Saša Bajt, Lars Gumprecht, Benedikt Rudek, Benjamin Erk, Carlo Schmidt, André Hömke, Christian Reich, Daniel Pietschner, Lothar Strüder, Günter Hauser, Hubert Gorke, Joachim Ullrich, Sven Herrmann, Gerhard Schaller, Florian Schopper, Heike Soltau, Kai-Uwe Kühnel, Marc Messerschmidt, John D Bozek, Stefan P Hau-Riege, Matthias Frank, Christina Y Hampton, Raymond G Sierra, Dmitri Starodub, Garth J Williams, Janos Hajdu, Nicusor Timneanu, M Marvin Seibert, Jakob Andreasson, Andrea Rocker, Olof Jönsson, Martin Svenda, Stephan Stern, Karol Nass, Robert Andritschke, Claus-Dieter

Schröter, Faton Krasniqi, Mario Bott, Kevin E Schmidt, Xiaoyu Wang, Ingo Grotjohann, James M Holton, Thomas R M Barends, Richard Neutze, Stefano Marchesini, Raimund Fromme, Sebastian Schorb, Daniela Rupp, Marcus Adolph, Tais Gorkhover, Inger Andersson, Helmut Hirsemann, Guillaume Potdevin, Heinz Graafsma, Björn Nilsson, and John C H Spence, *Femtosecond X-ray protein nanocrystallography.*, Nature **470** (2011), no. 7332, 73–7.

[14] JJ De Yoreo and P Vekilov, *Principles of crystal nucleation and growth*, Biomineralization **54** (2003), no. 57-93.

[15] Michael R DeFelippis, Diane L Bakaysa, Maureen A Bell, Mark A Heady, Shun Li, Susan Pye, Karen M Youngman, Jerry Radziuk, and Bruce H Frank, *Preparation and characterization of a cocrystalline suspension of [lysb28, prob29]-human insulin analogue*, Journal of pharmaceutical sciences **87** (1998), no. 2, 170–176.

[16] Sebastien Desbois, Shane A. Seabrook, and Janet Newman, *Some practical guidelines for UV imaging in the protein crystallization laboratory*, Acta Crystallographica Section F **69** (2013), no. 2, 201–208.

[17] Kaouthar Dhouib, Chantal Khan Malek, Wilhelm Pfleging, Bernard Gauthier-Manuel, Roland Duffait, Gaël Thuillier, Rosaria Ferrigno, Lilian Jacquamet, Jeremy Ohana, Jean-Luc Ferrer, Anne Théobald-Dietrich, Richard Giegé, Bernard Lorber, and Claude Sauter, *Microfluidic chips for the crystallization of biomacromolecules by counter-diffusion and on-chip crystal X-ray analysis.*, Lab on a Chip **9** (2009), no. 10, 1412–21.

[18] Richard D Dombrowski, James D Litster, Norman J Wagner, and Yinghe He, *Modeling the crystallization of proteins and small organic molecules in nanoliter drops*, AIChE Journal **56** (2010), no. 1, 79–91.

[19] RF Egerton, P Li, and M Malac, *Radiation damage in the tem and sem*, Micron **35** (2004), no. 6, 399–409.

[20] P Emsley and K Cowtan, *Coot:model-building tools for molecular graphics*, Acta Crystallographica Section D, Biological Crystallography **60** (2004), 2126–32.

[21] G. Entlicher, , J.V. Koštíř, and J. Kocourek, Biochimica et Biophysica Acta **236** (1971), 795–7.

[22] P.R. Evans, *An introduction to data reduction: space-group determination, scaling and intensity statistics*, Acta Crystallographica D **67** (2011), 282–292.

[23] Michael Faatz, Franziska Gröhn, and Gerhard Wegner, *Amorphous calcium carbonate: synthesis and potential intermediate in biomineralization*, Advanced Materials **16** (2004), no. 12, 996–1000.

[24] Geoffrey K Feld and Matthias Frank, *Enabling membrane protein structure and dynamics with x-ray free electron lasers*, Current opinion in structural biology **27** (2014), 69–78.

[25] Geoffrey K. Feld, Michael Heymann, W. Henry Benner, Tommaso Pardini, Ching-Ju Tsai, Sébastien Boutet, Matthew A. Coleman, Mark S. Hunter, Xiaodan Li, Marc Messerschmidt, Achini Opathalage, Bill Pedrini, Garth J. Williams, Bryan A. Krantz, Seth Fraden, Stefan Hau-Riege, James E. Evans, Brent W. Segelke, and Matthias Frank, *Low-Z polymer sample supports for fixed-target serial femtosecond X-ray crystallography*, Journal of Applied Crystallography **48** (2015), no. 4, 1072–1079.

[26] Matthias Frank, David B Carlson, Mark S Hunter, Garth J Williams, Marc Messerschmidt, Nadia A Zatsepin, Anton Barty, W Henry Benner, Kaiqin Chu, Alexander T Graf, et al., *Femtosecond x-ray diffraction from two-dimensional protein crystals*, IUCrJ **1** (2014), no. 2, 95–100.

[27] Oleg Galkin and Peter G. Vekilov, *Direct Determination of the Nucleation Rates of Protein Crystals*, The Journal of Physical Chemistry B **103** (1999), no. 49, 10965–10971.

[28] J. M. Garcia-Ruiz, *Nucleation of protein crystals. , 2003.*, Journal of Structural Biology **142** (2003), 22–31.

[29] J.M. Garcia-Ruiz, *Counterdiffusion methods for macromolecular crystallization*, Methods Enzymology **368** (2003), 130–154.

[30] Elspeth F. Garman, *Radiation damage in macromolecular crystallography: what is it and why should we care?*, Acta Crystallographica Section D **66** (2010), no. 4, 339–51.

[31] Denis Gebauer, Antje Völkel, and Helmut Cölfen, *Stable prenucleation calcium carbonate clusters*, Science **322** (2008), no. 5909, 1819–1822.

[32] Limay Goh, Kejia Chen, Venkateswarlu Bhamidi, Guangwen He, Nicholas C S Kee, Paul J a Kenis, Charles F Zukoski, and Richard D Braatz, *A Stochastic Model for Nucleation Kinetics Determination in Droplet-Based Microfluidic Systems.*, Crystal growth & design **10** (2010), no. 6, 2515–21.

[33] Sachit Goyal, Michael R. Thorson, Cassandra L. Schneider, Geoff G. Z. Zhang, Yuchuan Gong, and Paul J. A. Kenis, *A microfluidic platform for evaporation-based salt screening of pharmaceutical parent compounds*, Lab Chip **13** (2013), 1708–1723.

[34] Sachit Goyal, Michael R. Thorson, Geoff G. Z. Zhang, Yuchuan Gong, and Paul J. A. Kenis, *Microfluidic approach to cocrystal screening of pharmaceutical parent compounds*, Crystal Growth & Design **12** (2012), no. 12, 6023–6034.

[35] Sudipto Guha, Sarah L Perry, Ashtamurthy S Pawate, and Paul J A Kenis, *Chemical Fabrication of X-ray compatible microfluidic platforms for protein crystallization*, Sensors and Actuators B **174** (2012), 1–9.

[36] Carl L Hansen, Scott Classen, James M Berger, and Stephen R Quake, *A microfluidic device for kinetic optimization of protein crystallization and in situ structure determination.*, Journal of the American Chemical Society **128** (2006), no. 10, 3142–3.

[37] M. Heymann, S. Fraden, and D. Kim, *Multi-height precision alignment with selectively developed alignment marks*, Microelectromechanical Systems, Journal of **PP** (2013), no. 99, 1–4.

[38] Michael Heymann, *Microfluidic tools to investigate protein crystallization*, Ph.D. thesis, Brandeis University, 2014.

[39] Michael Heymann, Achini Opathalage, and Jennifer L. Wierman, *Room-temperature serial crystallography using a kinetically optimized microfluidic device for protein crystallization and on-chip x-ray diffraction*, IUCrJ (2014), 349–360.

[40] C Holtze, A C Rowat, J J Agresti, J B Hutchison, F E Angilè, C H J Schmitz, Sarah Köster, H Duan, K J Humphry, R A Scanga, J S Johnson, D Pisignano, and D A Weitz, *Biocompatible surfactants for water-in-fluorocarbon emulsions.*, Lab on a Chip **8** (2008), no. 10, 1632–9.

[41] Mark S Hunter, Brent Segelke, Marc Messerschmidt, Garth J Williams, Nadia A Zatsepin, Anton Barty, W Henry Benner, David B Carlson, Matthew Coleman, Alexander Graf, et al., *Fixed-target protein serial microcrystallography with an x-ray free electron laser*, Scientific reports **4** (2014).

[42] Manuel Ildefonso, Nadine Candoni, and Stéphane Veesler, *Heterogeneous Nucleation in Droplet-Based Nucleation Measurements*, Crystal Growth & Design **13** (2013), no. 5, 2107–2110.

[43] C. Jacobsen, J. Garside, and M. Hoare, *Nucleation and growth of microbial lipase crystals from clarified concentrated fermentation broths*, Biotechnology and Bioengineering **57** (1998), no. 6, 666–675.

[44] Jean L. Whittingham, § Ib Jonassen, § Svend Havelund, Shirley M. Roberts, Eleanor J. Dodson, Chandra S. Verma, , Anthony J. Wilkinson, , and G. Guy Dodson*, *Crystallographic and solution studies of n-lithocholyl insulin: a new generation of prolonged-acting human insulins*, Biochemistry **43** (2004), no. 20, 5987–5995, PMID: 15147182.

[45] C Kambach, S Walke, R Young, J M Avis, E de la Fortelle, V A Raker, R Lührmann, J Li, and K Nagai, *Crystal structures of two Sm protein complexes and their implications for the assembly of the spliceosomal snRNPs.*, Cell **96** (1999), no. 3, 375–87.

[46] D Kashchiev, *Nucleation: basic theory with applications. 2000.*

[47] D Kashchiev and GM Van Rosmalen, *Review: nucleation in solutions revisited*, Crystal Research and Technology **38** (2003), no. 7-8, 555–574.

[48] Ken Kelton and Alan Lindsay Greer, *Nucleation in condensed matter: applications in materials and biology*, vol. 15, Elsevier, 2010.

[49] Jan Kern, Roberto Alonso-Mori, Rosalie Tran, Johan Hattne, Richard J. Gildea, Nathaniel Echols, Carina Glöckner, Julia Hellmich, Hartawan Laksmono, Raymond G. Sierra, Benedikt Lassalle-Kaiser, Sergey Koroidov, Alyssa Lampe, Guangye Han, Sheraz Gul, Dörte DiFiore, Despina Milathianaki, Alan R. Fry, Alan Miahnahri, Donald W. Schafer, Marc Messerschmidt, M. Marvin Seibert, Jason E. Koglin, Dimosthenis Sokaras, Tsu-Chien Weng, Jonas Sellberg, Matthew J. Latimer, Ralf W. Grosse-Kunstleve, Petrus H. Zwart, William E. White, Pieter Glatzel, Paul D. Adams, Michael J. Bogan, Garth J. Williams, Sébastien Boutet, Johannes Messinger, Athina Zouni, Nicholas K. Sauter, Vittal K. Yachandra, Uwe Bergmann, and Junko Yano, *Simultaneous femtosecond x-ray spectroscopy and diffraction of photosystem ii at room temperature*, Science **340** (2013), no. 6131, 491–5.

[50] David J Kissick, Ellen J Gualtieri, Garth J Simpson, and Vadim Cherezov, *Nonlinear optical imaging of integral membrane protein crystals in lipidic mesophases.*, Analytical chemistry **82** (2010), no. 2, 491–7.

[51] Christopher Kupitz, Shibom Basu, Richard A. Kirian, Sadia Bari, Carl Caleman, Tzu-Chiao Chao, Katherine M. Davis, Lifen Yan, Yulia Pushkar, Lorenzo Galli, Stefan P. Hau-Riege, Matthias Frank, Stephan Kassemeyer, Stefano Marchesini, Andrew V. Martin, Ingo Grotjohann, Raimund Fromme, Kimberly N. Rendek, Jay-How Yang, and Danielle E. Cobb, *Serial time-resolved crystallography of photosystem ii using a femtosecond x-ray laser.*, Nature **513** (2014), no. 7517, 261 – 265.

[52] Liang Li, Debarshi Mustafi, Qiang Fu, Valentina Tereshko, Delai L Chen, Joshua D Tice, and Rustem F Ismagilov, *Nanoliter microfluidic hybrid method for simultaneous screening and optimization validated with crystallization of membrane proteins.*, Proceedings of the National Academy of Sciences of the United States of America **103** (2006), no. 51, 19243–8.

[53] Mengning Liang, Garth J. Williams, Marc Messerschmidt, M. Marvin Seibert, Paul A. Montanez, Matt Hayes, Despina Milathianaki, Andrew Aquila, Mark S. Hunter, Jason E. Koglin, Donald W. Schafer, Serge Guillet, Armin Busse, Robert Bergan, William Olson, Kay Fox, Nathaniel Stewart, Robin Curtis, Alireza Alan Miahnahri, and Sébastien Boutet, *The Coherent X-ray Imaging instrument at the Linac Coherent Light Source*, Journal of Synchrotron Radiation **22** (2015), no. 3, 514–519.

[54] Lukas Lomb, Thomas R. M. Barends, Stephan Kassemeyer, Andrew Aquila, Sascha W. Epp, Benjamin Erk, Lutz Foucar, Robert Hartmann, Benedikt Rudek, Daniel Rolles, Artem Rudenko, Robert L. Shoeman, Jakob Andreasson, Sasa Bajt, Miriam Barthelmess, Anton Barty, Michael J. Bogan, Christoph Bostedt, John D. Bozek, Carl Caleman, Ryan Coffee, Nicola Coppola, Daniel P. DePonte, R. Bruce Doak, Tomas Ekeberg, Holger Fleckenstein, Petra Fromme, Maike Gebhardt, Heinz Graafsma, Lars Gumprecht, Christina Y. Hampton, Andreas Hartmann, Günter Hauser, Helmut Hirsemann, Peter Holl, James M. Holton, Mark S. Hunter, Wolfgang Kabsch, Nils Kimmel, Richard A. Kirian, Mengning Liang, Filipe R. N. C. Maia, Anton Meinhart, Stefano Marchesini, Andrew V. Martin, Karol Nass, Christian Reich, Joachim Schulz, M. Marvin Seibert, Raymond Sierra, Heike Soltau, John C. H. Spence, Jan Steinbrener, Francesco Stellato, Stephan Stern, Nicusor Timneanu, Xiaoyu Wang, Georg Weidenspointner, Uwe Weierstall, Thomas A. White, Cornelia Wunderer, Henry N. Chapman, Joachim Ullrich, Lothar Strüder, and Ilme Schlichting, *Radiation damage in protein serial femtosecond crystallography using an x-ray free-electron laser*, Phys. Rev. B **84** (2011), 214111.

[55] Masatoshi Maeki, Hiroshi Yamaguchi, Kenichi Yamashita, Hiroyuki Nakamura, Masaya Miyazaki, and Hideaki Maeda, *Analysis of Kinetic Behavior of Protein Crystallization in Nanodroplets*, Chemistry Letters **40** (2011), no. 8, 825–827.

[56] ———, *A method for generating single crystals that rely on internal fluid dynamics of microdroplets*, Chem. Commun. **48** (2012), 5037–5039.

[57] Julia Mahamid, Barbara Aichmayer, Eyal Shimoni, Roy Ziblat, Chenghao Li, Stefan Siegel, Oskar Paris, Peter Fratzl, Steve Weiner, and Lia Addadi, *Mapping amorphous calcium phosphate transformation into crystalline mineral from the cell to the bone in zebrafish fin rays*, Proceedings of the National Academy of Sciences **107** (2010), no. 14, 6316–6321.

[58] Alexander J Malkin and Robert E Thorne, *Growth and disorder of macromolecular crystals: insights from atomic force microscopy and X-ray diffraction studies.*, Methods (San Diego, Calif.) **34** (2004), no. 3, 273–99.

[59] P. M. Martins, J. Pessoa, Z. Sàrkàny, F. Rocha, and A. M. Damas, *Rationalizing protein crystallization screenings through water equilibration theory and protein solubility data*, Crystal Growth & Design **8** (2008), no. 12, 4233–4243.

[60] Pedro M Martins, Fernando Rocha, and Ana M Damas, *Understanding water equilibration fundamentals as a step for rational protein crystallization*, PloS one **3** (2008), no. 4, e1998.

[61] J. C. McDonald, D. C. Duffy, J. R. Anderson, D. T. Chiu, H. Wu, O. J. A. Schueller, and G. M. Whitesides, *Fabrication of microfluidic systems in poly(dimethylsiloxane).*, Electrophoresis **21** (2000), 27–40.

[62] Alexander McPherson, *Crystallization of biological macromolecules*, Cold Spring Harbor Laboratory Press, 1999.

[63] G.N. Murshudov, P. Skubak, A.A. Lebedev, N.S. Pannu, R.A. Steiner, R.A. Nicholls, M.D. Winn, F. Long, and A.A. Vagin, *Refmac5 for the refinement of macromolecular crystal structures*, Acta Crystallographica D **67** (2011), 355–67.

[64] Brent L Nannenga and Tamir Gonen, *Protein structure determination by microed*, Current opinion in structural biology **27** (2014), 24–31.

[65] Richard Neutze, Remco Wouts, David van der Spoel, Edgar Weckert, and Janos Hajdu, *Potential for biomolecular imaging with femtosecond x-ray pulses*, Nature **406** (2000), no. 6797, 752–757.

[66] F. Otalora, J. A. Gavira, J. D. Ng, and J. M. Garcia-Ruiz, *Counterdiffusion methods applied to protein crystallization*, Progress in Biophysics and Molecular Biology **101** (2009), 26–37.

[67] Z. Otwinowski and W. Minor, *Processing of x-ray diffraction data collected in oscillation mode*, Methods in Enzymology: Macromolecular Crystallography, part A **276** (1997), no. 307–26.

[68] Bill Pedrini, Ching-Ju Tsai, Guido Capitani, Celestino Padeste, Mark S Hunter, Nadia A Zatsepin, Anton Barty, W Henry Benner, Sébastien Boutet, Geoffrey K Feld, et al., *7 å resolution in protein two-dimensional-crystal x-ray diffraction at linac coherent light source*, Philosophical Transactions of the Royal Society B: Biological Sciences **369** (2014), no. 1647, 20130500.

[69] ProtParam tool, http://web.expasy.org/protparam (2013).

[70] RAN Biotechnologies, http://www.ranbiotechnologies.com (2013).

[71] WS Rasband, Available from: http://imagej.nih.gov/ij (2013).

[72] L Redecke, K Nass, DP DePonte, TA White, D Rehders, A Barty, F Stellato, M Liang, TR Barends, S Boutet, GJ Williams, M Messerschmidt, MM Seibert, A Aquila, D Arnlund, S Bajt, T Barth, MJ Bogan, C Caleman, TC Chao, RB Doak, H Fleckenstein, M Frank, R Fromme, L Galli, I Grotjohann, MS Hunter, LC Johansson, S Kassemeyer, G Katona, RA Kirian, R Koopmann, C Kupitz, L Lomb, AV Martin, S Mogk,

R Neutze, RL Shoeman, J Steinbrener, N Timneanu, D Wang, U Weierstall, NA Zatsepin, JC Spence, P Fromme, I Schlichting, M Duszenko, C Betzel, and HN Chapman, *Natively inhibited trypanosoma brucei cathepsin b structure determined by using an x-ray laser*, Science **339** (2013), 227–30.

[73] Rigaku crystallization recipes, http://www.rigaku.com/products/protein/recipes (2013).

[74] Mark B Romanowsky, Adam R Abate, Assaf Rotem, Christian Holtze, and David A. Weitz, *High throughput production of single core double emulsions in a parallelized microfluidic device.*, Lab on a Chip **12** (2012), no. 4, 802–7.

[75] Sameer Talreja, Paul J. A. Kenis, *, , and § Charles F. Zukoski*, , *A kinetic model to simulate protein crystal growth in an evaporation-based crystallization platform*, Langmuir **23** (2007), no. 8, 4516–4522, PMID: 17367178.

[76] Tim Sanchez, Daniel T N Chen, Stephen J DeCamp, Michael Heymann, and Zvonimir Dogic, *Spontaneous motion in hierarchically assembled active matter.*, Nature **491** (2012), no. 7424, 431–4.

[77] Anna S. Schenk, Eduardo J. Albarracin, Yi-Yeoun Kim, Johannes Ihli, and Fiona C. Meldrum, *Confinement stabilises single crystal vaterite rods*, Chem. Commun. **50** (2014), 4729–4732.

[78] Jeremy D Schmit and Ken Dill, *Growth rates of protein crystals.*, Journal of the American Chemical Society **134** (2012), no. 9, 3934–7.

[79] Christian H J Schmitz, Amy C Rowat, Sarah Köster, and David A Weitz, *Dropspots: a picoliter array in a microfluidic device.*, Lab on a Chip **9** (2009), no. 1, 44–9.

[80] M Marvin Seibert, Tomas Ekeberg, Filipe RNC Maia, Martin Svenda, Jakob Andreasson, Olof Jönsson, Duško Odić, Bianca Iwan, Andrea Rocker, Daniel Westphal, et al., *Single mimivirus particles intercepted and imaged with an x-ray laser*, Nature **470** (2011), no. 7332, 78–81.

[81] Seila Selimović, Frédéric Gobeaux, and Seth Fraden, *Mapping and manipulating temperature-concentration phase diagrams using microfluidics.*, Lab on a Chip **10** (2010), no. 13, 1696–9.

[82] D Shi, BL Nannenga, MG Iadanza, and T Gonen, *elife, 2, e01345*, Web of Science (2013).

[83] Jung-Uk Shim, G. Cristobal, D.R. Link, T. Thorsen, Y. Jia, K. Piattelli, and S. Fraden, *Control and measurement of the phase behavior of aqueous solutions using microfluidics*, Journal of the American Chemical Society **129** (2007), 8825–35.

[84] Jung-Uk Shim, Galder Cristobal, Darren R Link, Todd Thorsen, and Seth Fraden, *Using Microfluidics to Decouple Nucleation and Growth of Protein Crystals.*, Crystal Growth & Design **7** (2007), no. 11, 2192–4.

[85] JCH Spence, U Weierstall, and HN Chapman, *X-ray lasers for structural and dynamic biology*, Reports on Progress in Physics **75** (2012), no. 10, 102601.

[86] Ralf Stehle, Guenter Goerigk, Dirk Wallacher, Matthias Ballauff, and Sebastian Seiffert, *Small-angle x-ray scattering in droplet-based microfluidics*, Lab Chip **13** (2013), 1529–1537.

[87] Francesco Stellato, Dominik Oberthür, Mengning Liang, Richard Bean, Cornelius Gati, Oleksandr Yefanov, Anton Barty, Anja Burkhardt, Pontus Fischer, Lorenzo Galli, Richard A. Kirian, Jan Meyer, Saravanan Panneerselvam, Chun Hong Yoon, Fedor Chervinskii, Emily Speller, Thomas A. White, Christian Betzel, Alke Meents, and Henry N. Chapman, *Room-temperature macromolecular serial crystallography using synchrotron radiation*, IUCrJ **1** (2014), no. 4.

[88] Christopher J. Stephens, Yi-Yeoun Kim, Stephen D. Evans, Fiona C. Meldrum, and Hugo K. Christenson, *Early stages of crystallization of calcium carbonate revealed in picoliter droplets*, Journal of the American Chemical Society **133** (2011), no. 14, 5210–5213, PMID: 21425847.

[89] Linzhi Tang and NY Lee, *A facile route for irreversible bonding of plastic-PDMS hybrid microdevices at room temperature*, Lab on a Chip **10** (2010), 1274–80.

[90] Jason Tenboer, Shibom Basu, Nadia Zatsepin, Kanupriya Pande, Despina Milathianaki, Matthias Frank, Mark Hunter, Sébastien Boutet, Garth J Williams, Jason E Koglin, et al., *Time-resolved serial crystallography captures high-resolution intermediates of photoactive yellow protein*, Science **346** (2014), no. 6214, 1242–1246.

[91] Chantel C. Tester, Michael L. Whittaker, and Derk Joester, *Controlling nucleation in giant liposomes*, Chem. Commun. **50** (2014), 5619–5622.

[92] Chantel C. Tester, Ching-Hsuan Wu, Steven Weigand, and Derk Joester, *Precipitation of acc in liposomes-a model for biomineralization in confined volumes*, Faraday Discuss. **159** (2012), 345–356.

[93] Joshua D Tice, Helen Song, Adam D Lyon, and Rustem F Ismagilov, *Formation of Droplets and Mixing in Multiphase Microfluidics at Low Values of the Reynolds and the Capillary Numbers*, Langmuir (2003), no. 11, 9127–9133.

[94] A. Vagin and A. Teplyakov, *Molrep: an automated program for molecular replacement*, Journal of Applied Crystallography **30** (1997), 1022–5.

[95] Peter G. Vekilov, *Nucleation*, Crystal Growth & Design **10** (2010), no. 12, 5007–5019.

[96] A. Vuolanto, S. Uotila, M. Leisola, and K. Visuri, *Solubility and crystallization of xylose isomerase from streptomyces rubiginosus.*, Journal of Crystal Growth **257** (2003), 404–11.

[97] Antti Vuolanto, Sinikka Uotila, Matti Leisola, and Kalevi Visuri, *Solubility and crystallization of xylose isomerase from streptomyces rubiginosus*, Journal of crystal growth **257** (2003), no. 3, 403–411.

[98] K. A. Walsh, *Trypsinogens and trypsins of various species.*, Methods in Enzymology **19** (1970), 41–63.

[99] Ronald D. Wampler, David J. Kissick, Christopher J. Dehen, Ellen J. Gualtieri, Jessica L. Grey, Hai-Feng Wang, David H. Thompson, Ji-Xin Cheng, and Garth J. Simpson, *Selective detection of protein crystals by second harmonic microscopy*, Journal of the American Chemical Society **130** (2008), no. 43, 14076–7.

[100] U Weierstall, JCH Spence, and RB Doak, *Injector for scattering measurements on fully solvated biospecies*, Review of Scientific Instruments **83** (2012), no. 3, 035108.

[101] Uwe Weierstall, Daniel James, Chong Wang, Thomas A White, Dingjie Wang, Wei Liu, John CH Spence, R Bruce Doak, Garrett Nelson, Petra Fromme, et al., *Lipidic cubic phase injector facilitates membrane protein serial femtosecond crystallography*, Nature communications **5** (2014).

[102] Britta Weinhausen and Sarah Köster, *Microfluidic devices for X-ray studies on hydrated cells.*, Lab on a Chip **13** (2013), no. 2, 212–5.

[103] L. R. Wetter and H. F. Deutsch, *Immunological studies on egg white proteins: Iv. immunochemical and physical studies of lysozyme*, Journal of Biological Chemistry **192** (1951), 237–42.

[104] Jennifer L. Wierman, Jonathan S. Alden, Chae Un Kim, Paul L. McEuen, and Sol M. Gruner, *Graphene as a protein crystal mounting material to reduce background scatter*, Journal of Applied Crystallography **46** (2013), no. 5, 1501–7.

[105] B. Zheng, L. S. Roach, and R. F. Ismagilov, *Screening of protein crystallization conditions on a microfluidic chip using nanoliter-size droplets*, Journal of the American Chemical Society **125** (2003), 11170–1.